Yb:Lu$_2$O$_3$ hydrothermally grown single-crystal high-resolution absorption spectra obtained between 8 and 300 K

David C. Brown[1] · Zackery Fleischman[2] · Larry D. Merkle[2] · Liurukara D. Sanjeewa[3] · Colin D. McMillen[4] · Joseph W. Kolis[4]

Abstract

We present new high-resolution absorption data for the important sesquioxide laser material Yb:Lu$_2$O$_3$ for the spectral range of 880–1020 nm, at various temperatures between 8 and 300 K, and for the zero-phonon region from 960 to 990 nm, at temperatures from 8 to 300 K. We have experimentally observed the C$_{3i}$ (0,1)–(1,3) transition for the first time, located at 880.7 nm at 8 K. Based on high confidence fitting functions to the experimental data, we provide the first complete compilation of all observed electronic and electronic–vibrational transitions. Detailed fitting and plots of the C$_2$ and C$_{3i}$ zero-line data show an evolution of the linewidth from being predominantly electronic below about 100 K to being dominated by thermal processes above 100 K. We have also found evidence for a "soft" phase transition between 80 and 100 K that changes the local coordination environment.

1 Introduction and background

Lutetia is one of three well-known isomorphic sesquioxide host crystals, Lu$_2$O$_3$, Y$_2$O$_3$, and Sc$_2$O$_3$, whose development has been recently driven by the Petermann and Huber groups at The University of Hamburg in Germany [1–3]. These crystals were developed as possible alternatives, with more favorable physical properties, to the well-developed legacy oxide host YAG (Y$_3$Al$_5$O$_{12}$). A number of experimental laser demonstrations have appeared in the literature, mostly exploring the usage of Yb:Lu$_2$O$_3$ as single crystals or transparent ceramics for CW and mode-locked lasers [4–12]. The high thermal stability, cubic structure, easy doping, and most importantly, the high thermal conductivity of the doped crystals make it an ideal material for extremely high-power solid-state cryolasers. A particular advantage of Lu$_2$O$_3$ over the other sesquioxide hosts Y$_2$O$_3$ and Sc$_2$O$_3$ is its retention of high thermal conductivity upon doping with Yb^{3+}, given the similarity in mass between Lu^{3+} and Yb^{3+} [5, 13]. To accelerate the design and development lutetia-based devices leveraging these advantages, a detailed understanding of the spectroscopy of the Yb^{3+} ions in this relatively novel lattice is essential. The results of previous collaborations by members of our group have appeared in a number of publications that focused primarily on Yb:Lu$_2$O$_3$ [14–16]. In [15] in particular, we presented Yb:Lu$_2$O$_3$ absorption measurements obtained at 80, 150, 200, 250, and 298 K. While we were able to successfully show the presence of the C$_{3i}$ site in the short wavelength shoulder of the main C$_2$ zero-phonon line at 976.21 nm, that became more pronounced as temperature was lowered, our data were noisy and we were unable to fully resolve the zero-phonon linewidth, or to lower the temperature any further. To further explore the variation of the overall spectral absorption, and particularly the evolution of the C$_{3i}$ and C$_2$ absorption features near the zero-phonon line, in this paper, we report the results of our collaboration with researchers at the US Army Research Laboratory whom were successful in obtaining very detailed high-resolution absorption data at a large number of temperatures from 8 to 300 K.

✉ David C. Brown
dbrown@apslasers.com

[1] Advanced Photonic Sciences, 26741 SR 267, Friendsville, PA 18818, USA

[2] US Army Research Laboratory, 2800 Powder Mill Road, Adelphi, MD 20783, USA

[3] Oak Ridge National Laboratory, Oak Ridge, TN 37830, USA

[4] Department of Chemistry and Center for Optical Materials Science and Engineering Technologies, Clemson University, Clemson, SC 29634-0973, USA

2 Lu₂O₃ crystal properties

For convenience, the crystalline properties of Lu_2O_3 are shown in Table 1 [1, 4, 17]. Lu_2O_3 is an optically isotropic host that provides a strong, robust, easily doped host for trivalent rare-earth ions, which substitute into body-centered Lu sites. Unlike YAG, however, which has one substitutable rare-earth site, Lu_2O_3 has two six-coordinated lutetium sites, with local point group symmetries of C_2 and C_{3i}. The former site has no inversion center, while the latter has a center of inversion. According to the LaPorte selection rule, electric dipole transitions are allowed in the C_2 site, while for the C_{3i} site, such transitions are forbidden. Indeed, this conclusion is found to be largely obeyed experimentally, where C_2 radiative sites predominate, while the C_{3i} transitions are much weaker. In this paper,

however, we show for the first time a systematic substantial variation in the strength of both the C_2 and C_{3i} site absorption as temperature is varied between 8 and 300 K, indicating that the local transition probability or oscillator strength of both sites change with temperature, likely due to changes in the local crystal field induced by slowly varying changes in the lattice parameter.

The Lu_2O_3 unit cell has been found to contain 32 cations, with 24 in the C_2 sites and 8 in the C_{3i} sites. In Table 1, we also provide nearest Lu–Lu inter-ion distances and Lu–O distances for both the C_2 and C_{3i} sites, as these are significant in the detailed spectral interpretation below. Figure 1 shows a structural rendering of the adjoining C_{3i} (left) and C_2 (right) Lu sites, with the site on the left having inversion symmetry, while the site on the right does not. In Fig. 2, the simple generic energy level structure of the Yb^{3+} ion in a crystalline host is shown; the $^2F_{7/2}$ ground-state consists

Table 1 Lu_2O_3 crystalline properties at 298 K

| Property	Value
Chemical formula	Lu_2O_3
Mineralogical structure type	Bixbyite
Scientific name	Lutetia
Transparency band gap (eV)	5.8
Formula Mass(g)	397.94
Density (g/cm³)	9.42
Crystal classification	Body-centered cubic
Optical class	Anaxial (isotropic)
Space group	$Ia\bar{3}$
Unit cell parameter (Å)	10.3971
Unit cell volume (Å³)	1123.9233
Number of unique cation sites (C_2 and C_{3i})	2
Metal ion site 1 point group symmetry C_2	Non-centrosymmetric
Metal ion site 2 point group symmetry C_{3i}	Centrosymmetric
C_2 emission properties: (non-centrosymmetric)	LaPorte rule allowed
C_{3i} emission properties: (centrosymmetric)	La Porte rule forbidden
Coordination ion	O
Coordination number	6
Number of formula units per unit cell	16
Number of Lu ions/unit cell	32
Number of O ions/unit cell	48
Total number of ions/unit cell	80
Number of Lu sites/unit cell with C_2 symmetry	24
Number of Lu sites/unit cell with C_{3i} symmetry	8
Ratio of number of C_2 to C_{3i} sites	3
Inter-ion distance from 8 Lu C_{3i} sites to 6 O sites (Å)	2.247
First inter-ion distance from 24 Lu C_2 sites to 2 O Sites (Å)	2.183
Second inter-ion distance from 24 Lu C_2 sites to 2 O Sites (Å)	2.239
Third inter-ion distance from 24 Lu C_2 sites to 2 O Sites (Å)	2.282
Lu C_{3i} to Lu C_{3i} inter-ion distance (Å)	5.195
Lu C_2 to Lu C_2 inter-ion distance (Å)	3.460
Lu C_{3i} to Lu C_2 inter-ion distance (Å)	3.433
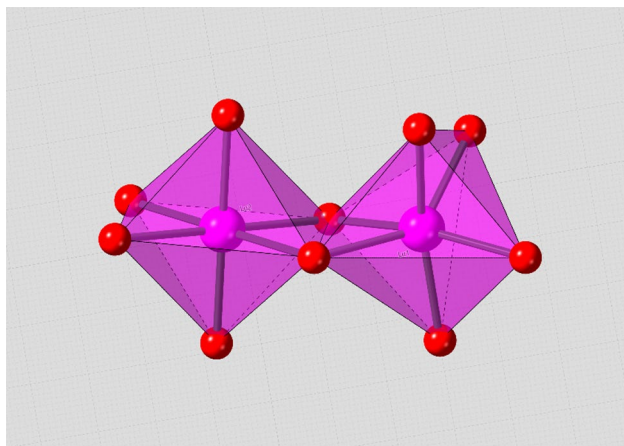
Fig. 1 Adjoining C$_{3i}$ (left) and C$_2$ (right) sites, showing Lu ions with sixfold O coordination
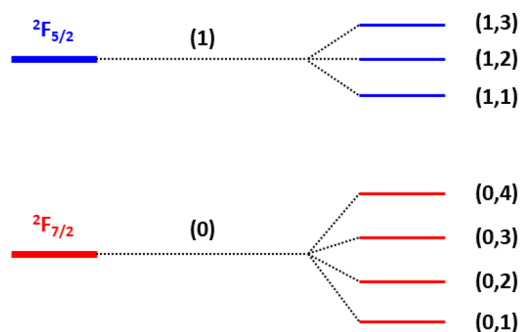

Yb:Host Energy Levels and Assignments

Fig. 2 Yb^{3+}:Host energy level manifolds

Fig. 3 Hydrothermally grown Yb:Lu$_2$O$_3$ crystal used in the present study

of four discrete Kramers doublet energy levels, while the $^2F_{5/2}$ excited-state consists of three Kramers doublet discrete levels. Also shown is the labeling of each level used in this paper.

3 Crystal growth and polishing

Crystal growth from hydrothermal solution took place in closed, pure silver reaction tubes containing the powdered feedstock along with aqueous mineralizer to dissolve and transport the material during the growth cycle. In the case of Yb:Lu$_2$O$_3$ discussed here, rare-earth oxide powders (HEFA Rare Earth, 99.997%) of Lu$_2$O$_3$ and Yb$_2$O$_3$ were measured in the desired doping ratio (3%) such that the total powdered material was approximately 1.5 g and added directly to ¼" OD × 7" long silver tubes that had been carefully cleaned, weld-sealed, and inspected for integrity. The powdered feedstock, along with 3 mL of a 20 M aqueous KOH
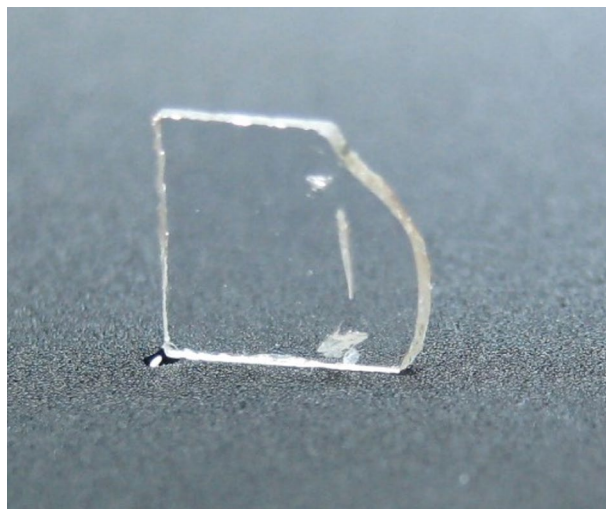
solution, was added before the tubes were welded closed. These loaded tubes were themselves inserted into Inconel autoclaves equipped with two external, individually controlled ceramic band heaters with temperature probes and pressure gauge assemblies to monitor temperatures and pressure throughout the entire growth process. Water added inside the autoclaves provides the counter pressure necessary to prevent bursting of reaction tubes when heated. The fully loaded and prepared autoclaves were then lowered into insulating pits and covered up to the pressure gauge in vermiculite. A temperature gradient was established with the band heaters of 670 °C for the top, growth zone, and 700 °C in the lower, dissolution zone, for this prograde solubility system. These temperatures typically resulted in pressures of around 207 MPa (30,000 psi). The autoclaves were left undisturbed in these insulated pits during the entire growth run of between 12 and 14 days. After this time, the heat was discontinued and autoclaves were left to cool naturally over several hours or quick-quenched by an air stream. The cooled reaction tubes were then carefully cut open to reveal various-sized single crystals of up to several mm on a side. While the temperature used in the present study represents a seemingly modest increase over our previous work [16], we observe improved faceting and a greater amount of optically clear regions in the as-grown crystals, compared to those grown at 630–650 °C. We postulate that moving the growth conditions farther away from the Lu$_2$O$_3$/LuO(OH) phase transition around 600 °C may be the source of such positive effects.

Crystals determined to be of sufficient optical quality for spectral analysis were further prepared, if necessary, by polishing. Progressive lapidary discs were used starting with 1200 grit and ending with 100,000 mesh diamond spray. The

crystal used in the present study was fabricated to dimensions of approximately $4 \times 4 \times 0.39$ mm, as shown in Fig. 3.

4 Absorption spectrophotometer and cryostat description

We performed very high-resolution absorption measurements using a Varian Cary 6000i UV–VIS–NIR absorption spectrophotometer that incorporated a CTI Cryodyne cryogenic refrigerator that included a heater, that was used to vary the absolute temperature between 8 and 300 K. The spectral resolution desired was set by computer control of the slit widths. For the Yb:Lu$_2$O$_3$ absorption data reported here, the spectral resolution was set to 0.15 nm for the broad scans, and to 0.05 nm for the narrow zero-line scans. The refrigerator contained two CaF$_2$ windows for the purpose of passing the absorbing beam through the cooled sample under high vacuum conditions to avoid water vapor condensation.

5 Yb:Lu$_2$O$_3$ experimental absorption data

In this paper, we present what we believe to be the first comprehensive set of high-resolution absorption data for Yb:Lu$_2$O$_3$ spanning the temperature range from 8 to 300 K. A thin hydrothermally grown 390 μm thick Yb:Lu$_2$O$_3$ single-crystal was prepared by careful polishing to avoid saturation of the zero-phonon line near 976 nm at low temperatures where the line intensities are substantially larger than at room temperature. The calculated crystal Yb^{3+} ion density was 3.0 at-%. In Sect. 5.1, we show obtained data in the wavelength interval from 880 to 1020 nm. The data were obtained with a spectral resolution of 0.15 nm, and a

sampling interval of 0.05 nm. In Sect. 5.2, we show detailed zero-line data around 976 nm, obtained with a spectral resolution of 0.05 nm and a sampling interval of 0.02 nm. All data reported in this paper are for wavelengths in air, and have not been converted to vacuum wavelengths.

5.1 Overview and discussion of absorption data from 880 to 1020 nm

Figures 4 and 5 plot the absorption coefficient as a function of wavelength for the absolute temperatures of 8, 30, 50, 75, 100, 150, 200, 250, and 300 K. Using the absorbance from the spectrophotometer, and correcting for the two Fresnel reflections of the Yb:Lu$_2$O$_3$ crystal using the Sellmeier equation of [18], and the four Fresnel reflections of the CaF$_2$ windows using the Sellmeier equation of [19], and the sample thickness, we obtained absorption coefficients for each temperature.

Transitions observed in the region from about 890–980 nm are attributable to three well-known transitions from the ground-state $^2F_{7/2}$ manifold to the sole excited-state $^2F_{5/2}$ manifold near 905 nm, 945 nm, and 975 nm [the (0,0) electronic zero-line]. Those transitions occur in Yb:Lu$_2$O$_3$ near 905 nm, 949 nm, and 976 nm as may be observed in Figs. 3, 4, 5, 6, 7, 8, 9, 10 and 11. A multitude of smaller peaks can be seen on the Stokes side of the 949 nm transition, and are likely electronic–vibrational in nature, with more than one vibrational mode contributing to the observed spectra. The sharp peak at 949.2 nm is the first (0, 1) vibrational zero-phonon line. Assuming that a number of vibrational modes contribute to the observed progressions, the peak at 949.2 nm is then viewed as the first zero (0–1) vibrational line with a phonon wing, followed by a number of additional (0–2),

Fig. 4 Yb:Lu$_2$O$_3$ absorption coefficient as a function of wavelength from 8 to 100 K

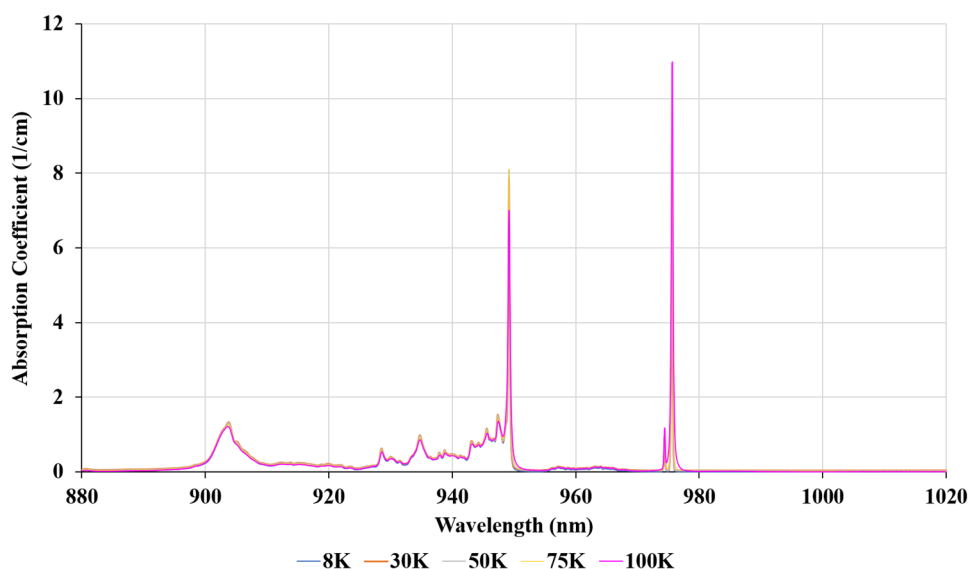**Fig. 5** Yb:Lu$_2$O$_3$ absorption coefficient as a function of wavelength from 100 to 300 K
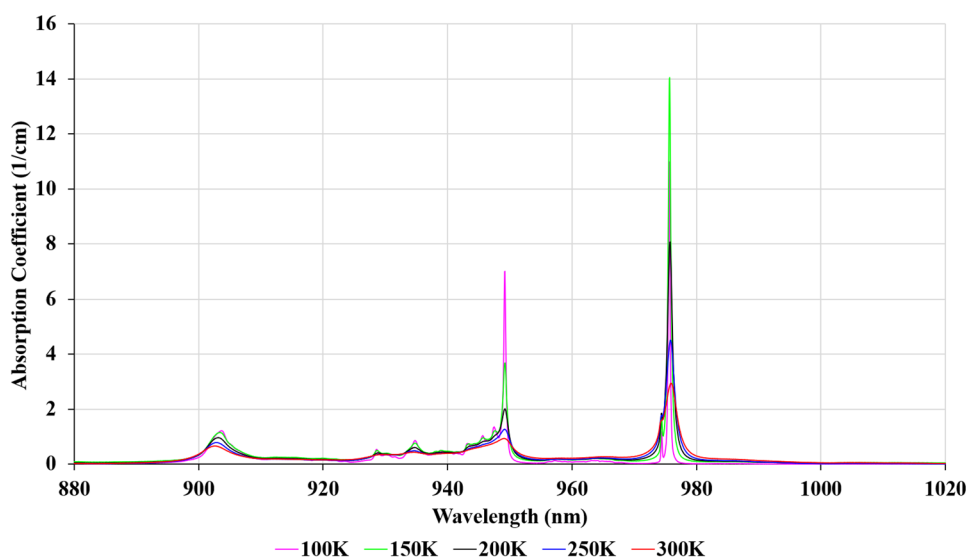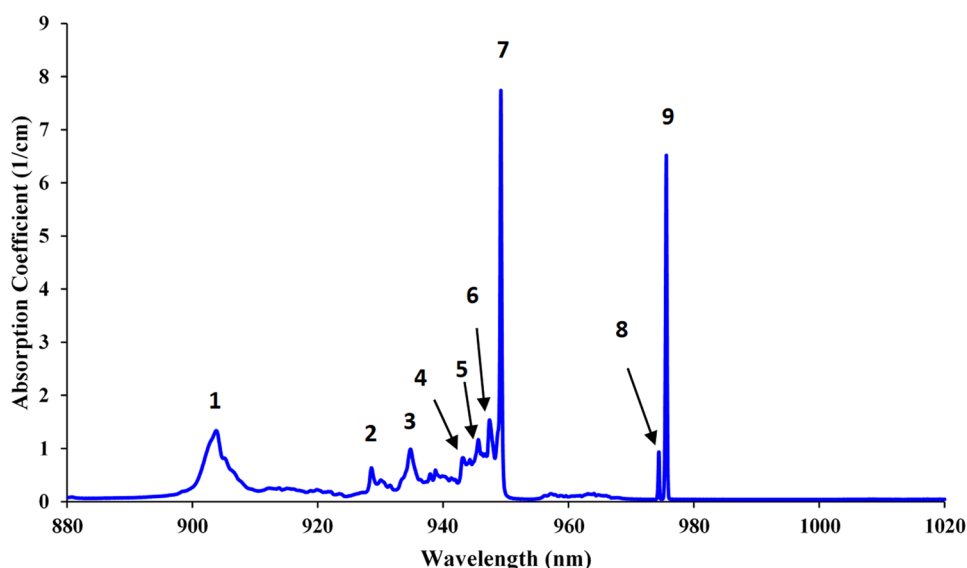

Fig. 6 Identification of nine peaks (peaks shown at 8 K here) examined for variation in amplitude and center wavelength with temperature

and perhaps (0–3) vibrational zero-lines and their phonon wings since the pure electronic zero-phonon line is common to all modes [20].

It is noteworthy that vibrational–electronic transitions are also observed on the anti-Stokes side of the 905 nm transition, albeit with much smaller amplitudes than those associated with the 949 nm transition. It is possible that those transitions are in fact an extension of the Stokes electronic-vibrational progressions associated with the 949 nm line. In addition, two weak broad (diffuse) transitions are observed at about 957.0 nm and 964.3 nm that have an unknown origin. Their proximity to the (0, 0) zero-phonon-line near 976 nm, however, suggests that a weak coupling between the zero-phonon electronic transition and an unknown vibrational mode may be occurring.

A number of interesting features can be observed as temperature is varied. The 905 nm transition is most well resolved at lower temperatures, and gradually (particularly above about 150 K) transitions to a more smoothed profile as temperature increases to 300 K. The center wavelength is nearly constant as the temperature increases, but above about 150 K the amplitude is diminished and the FWHM bandwidth increases substantially. For the 945 nm transition, the lines are best resolved at low temperatures, with all peaks having a near constant value up to about 100 K. At higher temperatures, the main peak as well as the secondary peaks diminish as temperature continues to rise. In addition, as with the 905 nm transition, all peaks display smoothing, an increase in FWHM bandwidth, and a substantial reduction in amplitude as temperature rises to 300 K.

Fig. 7 Variation in center wavelength with temperature for the nine peaks defined in Fig. 6
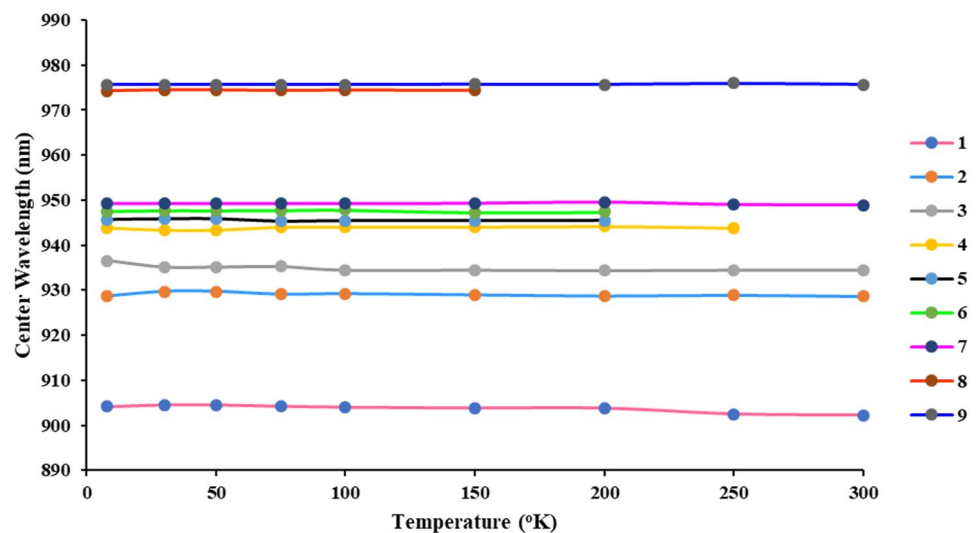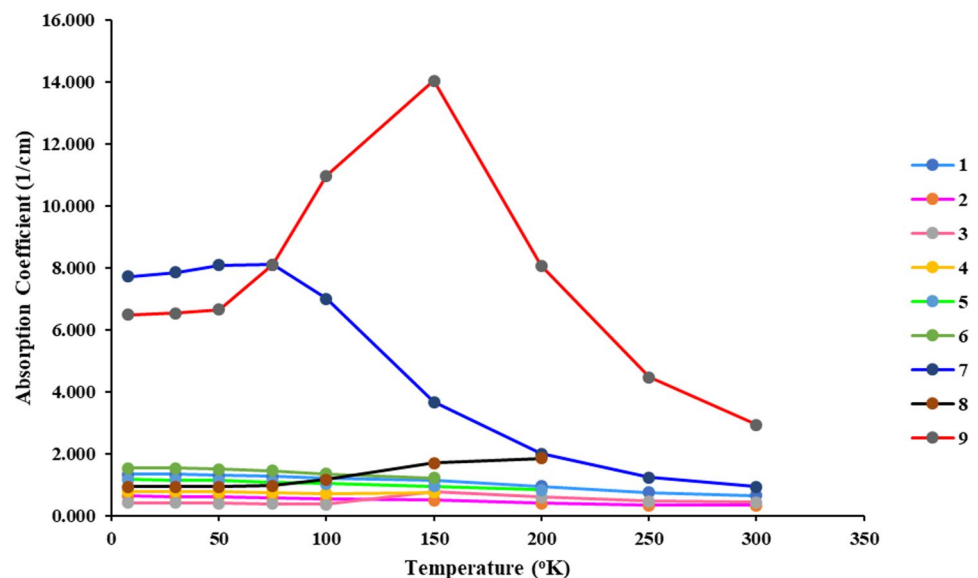

Fig. 8 Variation of absorption coefficient with temperature for the nine peaks defined in Fig. 6

The zero-line at about 976 nm displays the most interesting behavior. There are two distinct lines in the region that can be observed from 8 K all the way up to 300 K. The smaller line has been previously identified as the C_{3i} zero-phonon line [1]. That substantial intensity is observed is due to LaPorte's rule not being completely satisfied for the C_{3i} site (i.e. it does not identically have complete inversion symmetry). The obtained data show conclusively that the C_{3i} and the C_2 lines remain adjacent throughout the entire temperature range, and that at about 75 K appear to begin merging, a process that continues to 300 K. The merging, however, appears to be due to the increased linewidth of the C_2 transition, as well as to the increased amplitude. The C_2 transition displays an amplitude that is nearly constant up to about 75 K; thereafter, the amplitude rapidly increases until 150 K, and then continuously decreases up to 300 K. We observed this behavior previously [15], but the higher resolution data presented here allow a much more detailed look at the evolution of both the C_{3i} and C_2 sites as temperature is varied over a wide range. Up to liquid nitrogen temperature near 77 K, the C_{3i} and C_2 sites can be assumed to be mostly independent of one another, and cross-sections can be assigned to each since the C_{3i} contains ¼ of all Yb ions, and the C_2 site ¾. At room temperature, however, the merging of the absorption transitions of both sites means that both contribute to the total absorption and a means of assigning the contribution of each can produce good fitting functions to the observed profiles.

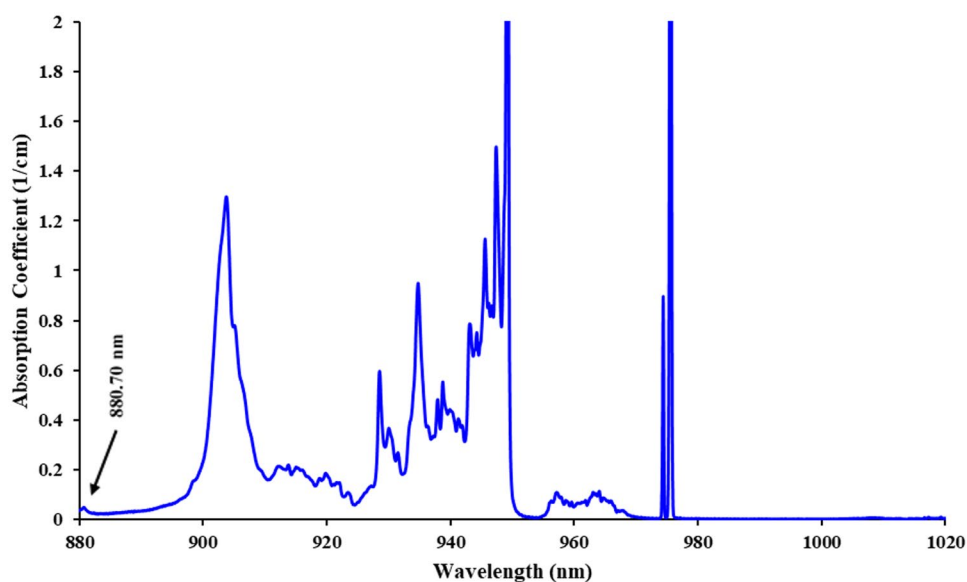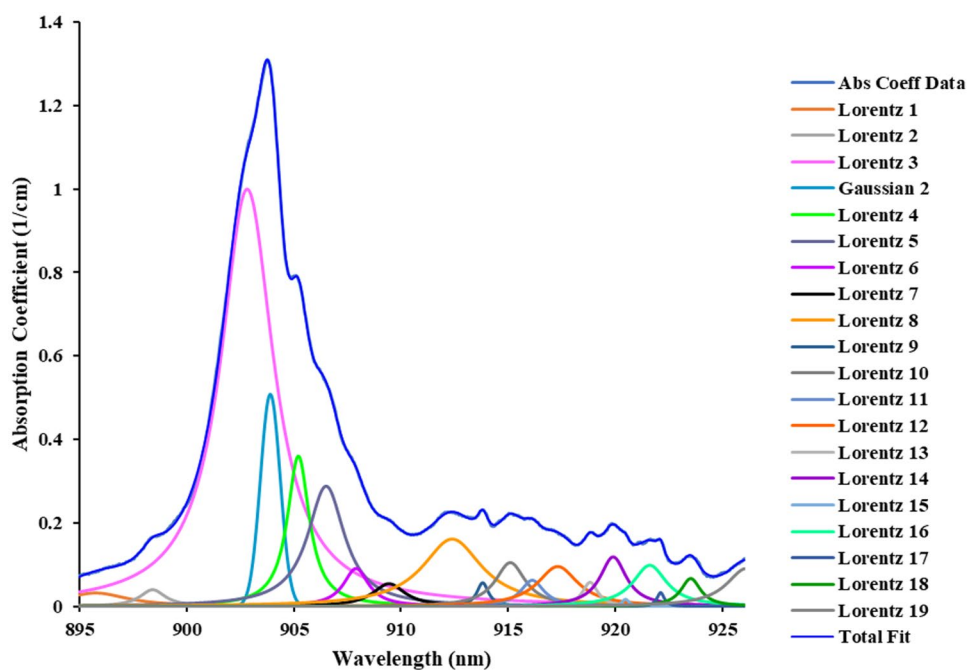**Fig. 9** Identification of C$_{3i}$ (0, 1)–(1, 3) transition at 880.7 nm at 8 K

Fig. 10 All fitting functions identified to reproduce experimental Yb:Lu$_2$O$_3$ absorption coefficient data from 895 to 926 nm at 8 K with high confidence

5.2 Variation of center wavelength and amplitudes with temperature

In Fig. 6, we identify nine lines in the 880–980 nm region that we chose to examine to determine the variation in the center wavelength and amplitude with temperature. The nine lines include the three $^2F_{7/2}$–$^2F_{5/2}$ electronic absorption transitions (1, 7, 9), the major electronic-vibronic transitions (2, 3, 4, 5, 6), both associated with the C$_2$ site, and the C$_{3i}$ zero-phonon transition (8). Table 2 shows the measured values for the center wavelength for nine temperatures for each of the lines. Also shown are the

average value, the standard deviation, and the percent variation over the temperature interval. Note that for lines 4, 5, 6, and 8, wavelength values could not be determined beyond that temperature at which the line became difficult to measure because the amplitude had merged with the growing background. Figure 7 is a plot of the variation of the center wavelength with temperature, and used the data of Table 2. The standard deviations and percent change over the temperature intervals are seen to be very small for all nine lines. The C$_{3i}$ zero-phonon line (8) has no variation with temperature at all, and the C$_2$ zero-phonon line has a very small change. Line 1 displays a relatively large

Fig. 11 Yb:Lu$_2$O$_3$ vibrational transitions identified in the 895–926 nm spectral region
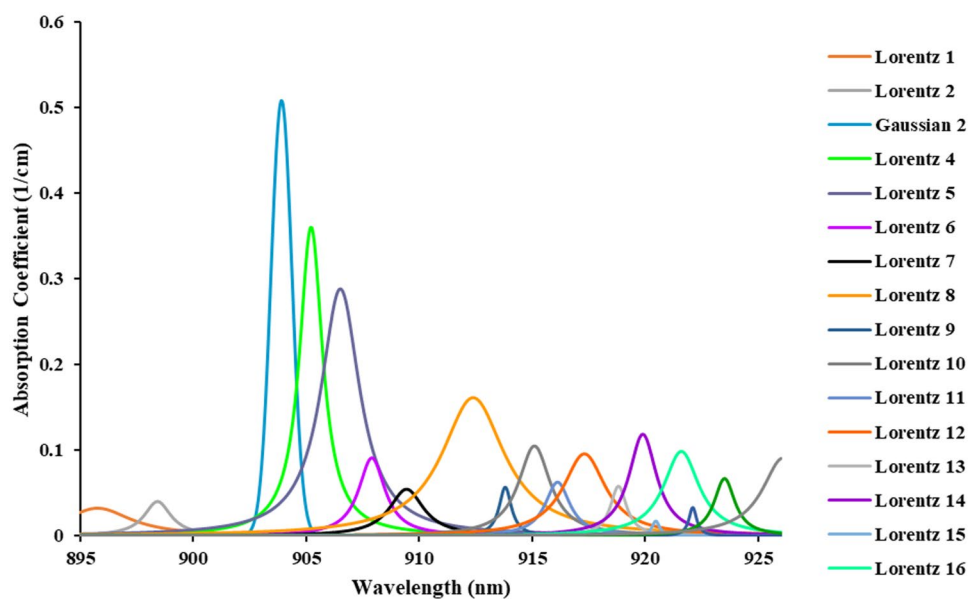

Table 2 Variation of center wavelength with temperature for nine major peaks

Peak	1	2	3	4	5	6	7	8	9
T (K)									
8	903.80	928.55	936.30	944.25	945.60	947.40	949.20	974.40	975.60
30	903.75	928.55	936.30	944.25	945.60	947.40	949.20	974.40	975.60
50	903.75	928.55	936.30	944.25	945.60	947.70	949.20	974.40	975.60
75	903.75	928.60	936.25	944.30	945.55	947.40	949.20	974.40	975.60
100	903.70	928.60	936.35	944.30	945.65	947.45	949.20	974.40	975.60
150	903.40	928.70	934.80	944.40	945.75	947.65	949.20	974.40	975.70
200	903.15	928.80	934.80		945.80		949.20	974.40	975.75
250	902.85	929.05	934.65				949.20		975.80
300	902.80	929.10	934.65				949.05		975.95
Avg	903.44	928.72	935.60	944.29	945.65	947.50	949.18	974.40	975.69
SD	0.41	0.22	0.83	0.06	0.09	0.14	0.05	0.00	0.12
%	0.05	0.02	0.00	0.01	0.01	0.02	0.01	0.00	0.01

Table 3 Variation of absorption coefficient with temperature for the nine major peaks

Peak	1	2	3	4	5	6	7	8	9
T (K)									
8	1.337	0.637	0.417	0.792	1.168	1.538	7.728	0.935	6.492
30	1.330	0.629	0.414	0.788	1.162	1.531	7.856	0.932	6.540
50	1.312	0.615	0.404	0.776	1.143	1.508	8.092	0.934	6.662
75	1.277	0.587	0.392	0.757	1.083	1.447	8.103	0.968	8.108
100	1.217	0.536	0.374	0.730	1.039	1.351	6.998	1.178	10.972
150	1.151	0.498	0.765	0.750	0.961	1.215	3.676	1.704	14.037
200	0.963	0.407	0.605		0.832		2.007	1.861	8.070
250	0.760	0.331	0.465				1.246		4.473
300	0.656	0.346	0.436				0.935		2.942

change in wavelength with temperature, and the vibrational line 3 the largest change.

Table 3 shows the variation of the absorption coefficient with temperature for all nine lines; the data are all plotted in Fig. 8. The most pronounced variation was found for the C$_2$ zero-phonon line (9), that began to increase at about 50 K, peaks at about 150 K, and then continuously decreases to 300 K. The C$_{3i}$ zero-phonon line (8) also increased with temperature starting at about 75 K, and then increased up until 200 K. A large variation is also seen in line 7, the zero-phonon vibrational line, which increases up to about 75 K, and then continuously decays as the temperature increases. The remaining lines (1–6) display minor changes with temperature, with all decreasing above about 150 K. In general, lines 2–6 are associated with vibrational bands with amplitudes that decrease with temperature above about 50–75 K. The C$_2$ and C$_{3i}$ zero-phonon lines, however, undergo changes that seem to be primarily thermally driven above about 150–200 K. From the lowest temperatures to 150–200 K, however, the amplitudes grow significantly, indicating that important changes (distortions) in the local crystalline field are taking place. In Sect. 5.6 of this paper, we present more detained data for the zero-phonon lines at 15 temperatures, and further examine this point.

5.3 Determination of Yb:Lu$_2$O$_3$ energy levels and comparison to previously obtained results

In Table 4, we show the energies of the four (0, 1), (0, 2), (0, 3), and (0, 4) $^2F_{7/2}$ levels in the ground-state manifold and the three (1, 1), (1, 2), and (1, 3) levels in the $^2F_{5/2}$ excited-state manifold, obtained from a number of prior publications at the temperatures shown. All values have units of (cm^{-1}). Rows 1 and 2 show the results reported in the Dissertation of Peters [2] for both the C$_2$ and C$_{3i}$ sites, but at unknown temperatures (U). The most recent tabulation of values, found in the paper by Guyot et al.[21], are shown in rows 3–4 for the C$_2$ and C$_{3i}$ sites, respectively, at 10 K. We also show in rows 5 and 6 values for the (1, 1) level in both the C$_2$ and

C$_{3i}$ sites, as reported by Petermann at 10 K [3]. Finally, we show values for the (1, 1), (1, 2), and (1, 3) C$_2$ and C$_{3i}$ levels in rows 7 and 8 as determined by the authors of the present paper at 8 K. The energy levels quoted by Guyot et al. [21] align very closely to our values, and in rows 9 and 10, we show the differences between our values and those of [21] for C$_2$ (ΔC$_2$) and C$_{3i}$ (ΔC$_{3i}$), respectively. The energies agree particularly well for the C$_2$ site, although the C$_{3i}$ energy levels are close as well. The maximum disagreement for the (1, 3) levels amounts to only 0.15%.

The values we determined for the zero-phonon line C$_2$ and C$_{3i}$ sites of 10,250.10 and 10,262.73 cm^{-1} were obtained from the data of Table 2 at 8 K. By comparison of our absorption data with that of [21], we expected to find a low-intensity line at 882.07 nm. Close examination of the baseline data of Fig. 3 yielded the peak shown in Fig. 9 at 8 K, which we determined to be located at 880.70 nm. To measure the (1, 2) energy for the C$_2$ site at 8 K, we use the value shown in Table 2 of 949.2 nm, (10,535.19 cm^{-1}). To identify the C$_{3i}$ energy for the (1, 2) level, we used a complete fit of all the electronic and phonon transitions in the range of 925–955 nm discussed in Sect. 5.4 of this paper. Again, using the previously published value of [21], we expected to see a transition at about 942.06 nm; examination of the fits shown later in Fig. 12 revealed a low-intensity transition at 941.4 nm, or 10,622.48 cm^{-1}. It should be noted that the location of the (1, 3) line is not exactly at 903.80 nm; the real location is 903.907 nm, since it should likely have a Gaussian linewidth as do the other C$_2$ (1, 1) and (1, 2) transitions.

5.4 Detailed fitting of All Yb:Lu$_2$O$_3$ transitions outside zero-phonon line region at 8 K

5.4.1 Fitting functions and peak identification for Yb:Lu$_2$O$_3$ 825–926 nm region

We performed extensive interactive fits of all the peaks identified in the 825–956 nm spectral region that contains the C$_2$ (0, 1)—(1, 3) electronic transition as well as

Table 4 Energy levels of Yb:Lu$_2$O$_3$

T (K)		(0, 1)	(0, 2)	(0, 3)	(0, 4)	(1, 1)	(1, 2)	(1, 3)	References
U	C$_2$	0	427	514	903	10,244	10,666	11,073	[2]
U	C$_{3i}$	0	112	333	1157	10,257	10,377	11,319	[2]
477	C$_2$	0	301	563	988	10,251	10,537	11,071	[21]
477	C$_{3i}$	0	299	859	1193	10,264	10,615	11,337	[21]
10	C$_2$	0				10,235			[3]
10	C$_{3i}$	0				10,248			[3]
8	C$_2$	0				10,250.10	10,535.19	11,063.09	[Here]
8	C$_{3i}$	0				10,262.73	10,622.48	11,354.60	[Here]
ΔC$_2$						0.90	1.81	− 7.91	
ΔC$_{3i}$						1.27	− 7.48	− 17.60	

Fig. 12 All fitting functions identified to reproduce experimental Yb:Lu_2O_3 absorption coefficient data from 925 to 954 nm at 8 K with high confidence
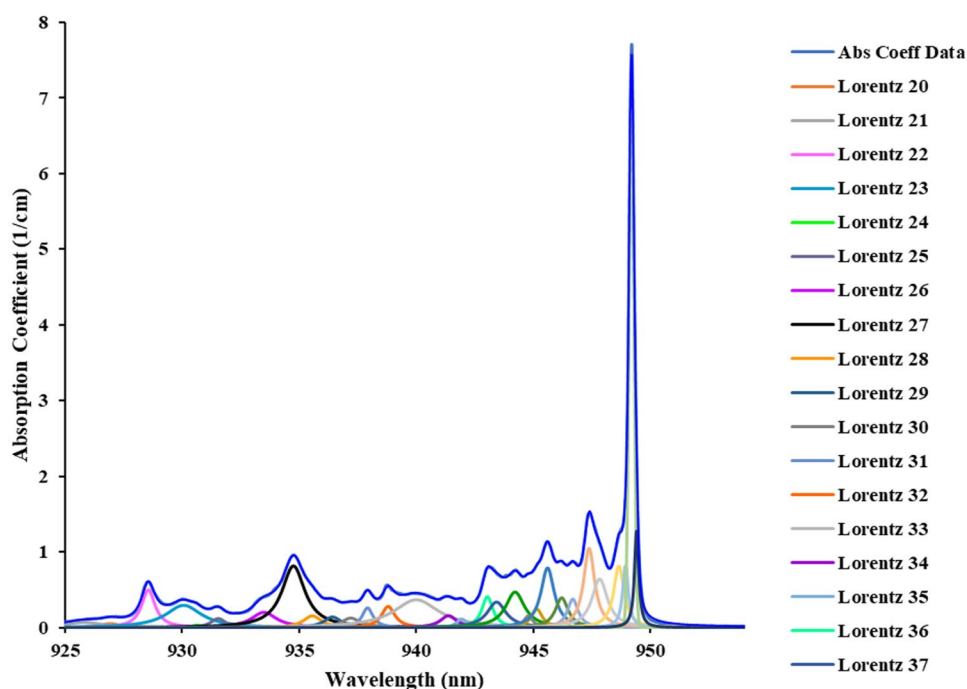
a multitude of electronic-vibrational transitions. Most of our fits were generated using Fityk, which enables users to specify any number of standard fitting functions including Gaussian, Lorentzian, Voight, Pearson, and many others. In the work described here, for simplicity we restricted ourselves to standard Gaussian and Lorentzian functions only, and found that more than adequate results could be obtained with excellent chi-squared fitting values.

Figure 10 shows the obtained results: plots of the experimental data, each transition used to fit the total curve, and the resulting total fit which is nearly indistinguishable from the starting absorption coefficient data. The χ^2 value obtained for this set of functions was 99.986%. The best overall fit was found to contain one Gaussian and 19 Lorentzian functions. It should be pointed out, however, that while the fit shown here is very good, there is no guarantee of uniqueness and many other fits may exist that give similar results. Our purpose here is thus to provide one set of functions that fit the experimental data very well, that other researchers may use as a guide in developing a more rigorous approach. In Table 5, we show the transition number, the fitting function type and number, the center wavelength, peak absorption coefficient, FWHM bandwidth, and the center wavenumber for each fitting transition used, and have added the C_{3i} transition at 880.677 nm (transition number 1) as well, that was found to be best fitted as a Gaussian with the parameters shown. Transition number 4 corresponds, we believe, to the C_2 (0, 1)–(1, 3) transition. If we remove the total absorption coefficient, the fit to the absorption coefficient, and the C_2 transition,

the remaining transitions are shown in Fig. 11, and are believed to be primarily electronic-vibrational in origin.

5.4.2 Fitting functions and peak identification for Yb:Lu_2O_3 925–954 nm region

We performed the same type of fitting analysis of the 925–954 nm region (Fig. 12). Table 6 shows the various Lorentzian and Gaussian functions used and their parameters The χ^2 value obtained for this set of functions was 99.950%. A total of 30 Lorentzian functions and a single Gaussian function were used. After removing the electronic functions, the results shown in Fig. 13 are obtained: all transitions are believed to be electronic–vibrational in nature.

5.5 Yb:Lu_2O_3 electronic–vibrational transitions

It has been noted in the literature [22] that Yb-doped laser materials display strong electron–phonon coupling, as do a number of other ions at the beginning and end of the lanthanide series. A decrease in the shielding of the 4f electrons by 5 s and 5p is considered to be the main factor for the large electron–phonon coupling for Yb^{3+}. It has also been pointed out that Stark splittings of rare-earth ions in crystals are on the order of typical lattice optical phonon, so that in addition to normal electron–phonon coupling, near-resonance processes may appear and couple the vibronic state associated with one electronic level to those of another.

Here, we see that for Yb:Lu_2O_3, the vibrational structure is rich and dense. Through detailed modeling with

Table 5 Yb:Lu$_2$O$_3$ electronic and vibrational transitions from 880 to 926 nm

Transition number	Fitting function type	Center wavelength (nm)	Absorption coefficient (1/cm)	FWHM bandwidth (nm)	Center wavenumber (cm^{-1})
1	Gaussian 1	880.677	0.022	1.263	11,354.901
2	Lorentzian 1	895.770	0.032	3.640	11,163.580
3	Lorentzian 2	898.424	0.040	1.440	11,130.602
4	Lorentzian 3	902.830	1.000	2.980	11,076.282
5	Gaussian 2	903.907	0.508	1.086	11,063.085
6	Lorentzian 4	905.215	0.360	1.244	11,047.099
7	Lorentzian 5	906.509	0.288	2.094	11,031.330
8	Lorentzian 6	907.902	0.091	1.418	11,014.405
9	Lorentzian 7	909.434	0.055	1.840	10,995.850
10	Lorentzian 8	912.382	0.162	3.368	10,960.321
11	Lorentzian 9	913.802	0.057	0.662	10,943.290
12	Lorentzian 10	915.092	0.105	1.702	10,927.863
13	Lorentzian 11	916.115	0.063	1.328	10,915.660
14	Lorentzian 12	917.301	0.096	2.290	10,901.547
15	Lorentzian 13	918.810	0.058	0.874	10,883.643
16	Lorentzian 14	919.885	0.119	1.492	10,870.924
17	Lorentzian 15	920.460	0.017	0.414	10,864.133
18	Lorentzian 16	921.589	0.099	1.908	10,850.824
19	Lorentzian 17	922.094	0.033	0.416	10,844.881
20	Lorentzian 18	923.499	0.067	1.120	10,828.382

fitting software, we identified the many (46) vibrational lines in the Yb:Lu$_2$O$_3$ absorption spectral region from 880 to 954 nm at 8 K by subtracting out the known C$_2$ and C$_{3i}$ electronic transitions. A detailed analysis of the observed vibrational lines using the formulation of [22] could likely yield insights into the observed vibrational structure, but such an analysis is beyond the scope of this paper. There are, however, a number of interesting features that we will point out here. First, the vibrational lines are all (with the exception of the two small diffuse bands observed) observed to occur between the (0, 1)–(1, 2) and (1, 3) electronic transitions at 949.19 and 902.83 nm, with the largest number of transitions found closer to the 949.19 nm line. The vibrational lines are Stokes shifted from the 949.19 nm line, and anti-Stokes with respect to the 902.83 nm line. Because anti-Stokes lines are less probable than Stokes lines, it is possible that most of the observed vibrational lines originate from the coupling of multiple vibrational modes to the (0, 1)–(1, 2) electronic transition. In addition, multiple vibrational modes can produce additional modes with energies at multiples of the fundamental vibrational frequencies. Compilations of the Raman-determined modes, including those at most fundamental modes have been tabulated in [23, 24] for Lu$_2$O$_3$, and span the wavenumber range from 65 to 612 cm^{-1}. The line at 949.189 nm is very likely the first vibrational (0,1) zero-phonon line, and the peaks identified as lines 4, 5,

and 6 in Fig. 6 are likely part of the phonon tail; lines 2 and 3 may be additional vibrational zero-phonon lines (0, 2) and (0, 3), also with accompanying phonon tails. The wavenumber difference between the 949.19 nm and 902.83 nm transitions is about 541 cm^{-1}, or close to an F$_g$ vibration at 499 cm^{-1}, and twice a known vibration at 264 cm^{-1}.

To help identify the origin of the vibrational modes, Table 7 lists all the identified vibrational modes in the spectral region between 880 and 949.189 nm, the associated wavelengths and wavenumbers, the vibrational offset between the vibrational mode and the zero-vibrational mode at 949.190 nm, and the known Raman-determined vibrational modes for Lu$_2$O$_3$. Several of the offsets are very close to known vibrational modes. Without detailed modeling of the coupled electronic and vibrational states, however, we cannot be certain whether the near agreement between the offsets and known vibrational modes is simply fortuitous or has a deeper foundation.

Finally, it is notable there are no significant vibrational modes associated with the zero-phonon line at 975.584 nm, although as we shall discuss in Sect. 5.6 of this paper, the zero-line at low temperatures can be fit to show the existence of three separate lines, one Gaussian believed to be the electronic transition, and two additional Lorentzian lines whose origin we discuss.

Table 6 Yb:Lu$_2$O$_3$ electronic and vibrational transitions from 925 to 954 nm

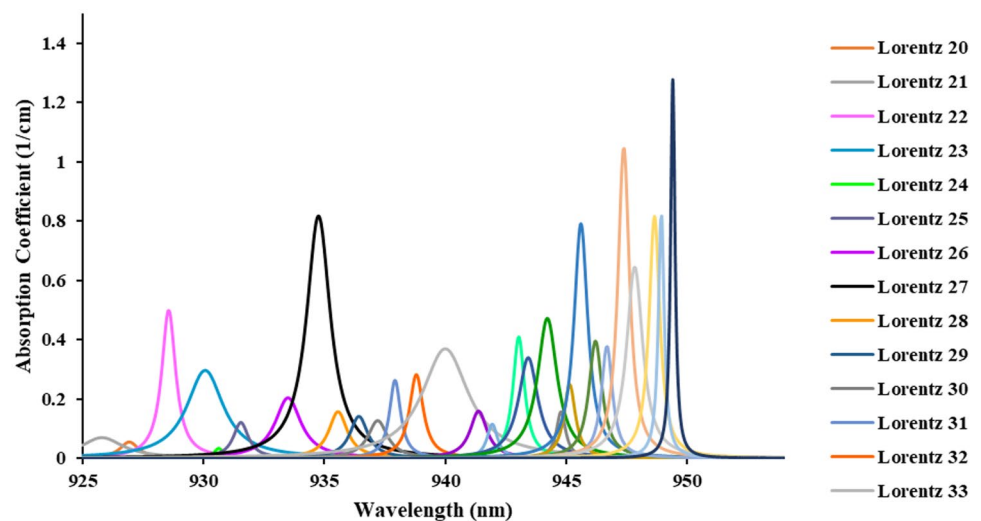| Transition number	Fitting function type	Center wavelength (nm)	Absorption coefficient (1/cm)	FWHM bandwidth (nm)	Center wavenumber (cm^{-1})
21	Lorentzian 19	926.096	0.091	2.254	10,798.017
22	Lorentzian 20	926.938	0.055	0.940	10,788.208
23	Lorentzian 21	925.809	0.070	2.118	10,801.364
24	Lorentzian 22	928.568	0.499	0.700	10,769.271
25	Lorentzian 23	930.075	0.297	1.842	10,751.821
26	Lorentzian 24	930.636	0.033	0.452	10,745.340
27	Lorentzian 25	931.551	0.121	0.758	10,734.785
28	Lorentzian 26	933.500	0.204	1.298	10,712.373
29	Lorentzian 27	934.760	0.817	1.200	10,697.933
30	Lorentzian 28	935.567	0.157	0.932	10,688.705
31	Lorentzian 29	936.429	0.142	0.900	10,678.866
32	Lorentzian 30	937.207	0.127	0.980	10,670.001
33	Lorentzian 31	937.923	0.264	0.556	10,661.856
34	Lorentzian 32	938.804	0.282	0.688	10,651.851
35	Lorentzian 33	940.000	0.369	2.334	10,638.298
36	Lorentzian 34	941.375	0.159	0.850	10,622.759
37	Lorentzian 35	941.942	0.115	0.526	10,616.365
38	Lorentzian 36	943.036	0.410	0.578	10,604.049
39	Lorentzian 37	943.429	0.339	0.974	10,599.632
40	Lorentzian 38	944.218	0.472	0.986	10,590.775
41	Lorentzian 39	944.784	0.158	0.464	10,584.430
42	Lorentzian 40	945.141	0.249	0.572	10,580.432
43	Lorentzian 41	945.605	0.791	0.692	10,575.240
44	Lorentzian 42	946.208	0.395	0.666	10,568.501
45	Lorentzian 43	946.681	0.378	0.558	10,563.220
46	Lorentzian 44	947.378	1.050	0.572	10,555.449
47	Lorentzian 45	947.829	0.645	0.812	10,550.426
48	Lorentzian 46	948.647	0.816	0.538	10,541.329
49	Lorentzian 47	948.930	0.831	0.290	10,538.185
50	Gaussian 3	949.189	6.868	0.250	10,535.310
51	Lorentzian 48	949.405	1.279	0.218	10,532.913

Fig. 13 Vibrational transitions identified from 925 to 954 nm

Table 7 Vibrational wavenumber offset from zero vibrational line at 949.19 nm for all vibrational transitions identified, and comparison to closest known Raman-identified vibrational modes

Transition number	Fitting function type	Center wavelength (nm)	Center wavenumber (cm^{-1})	Vibrational offset (cm^{-1})	Closest vibrational mode (cm^{-1})
2	Lorentzian 1	895.770	11,163.580	628.270	612.00
3	Lorentzian 2	898.424	11,130.602	595.292	612.00
4	Lorentzian 3	902.830	11,076.282	540.972	
6	Lorentzian 4	905.215	11,047.099	511.789	
7	Lorentzian 5	906.509	11,031.330	496.020	499.00
8	Lorentzian 6	907.902	11,014.405	479.095	
9	Lorentzian 7	909.434	10,995.850	460.540	454.00
10	Lorentzian 8	912.382	10,960.321	425.011	
11	Lorentzian 9	913.802	10,943.290	407.980	
12	Lorentzian 10	915.092	10,927.863	392.553	393.00
13	Lorentzian 11	916.115	10,915.660	380.350	
14	Lorentzian 12	917.301	10,901.547	366.237	368.00
15	Lorentzian 13	918.810	10,883.643	348.333	348.00
16	Lorentzian 14	919.885	10,870.924	335.614	
17	Lorentzian 15	920.460	10,864.133	328.823	
18	Lorentzian 16	921.589	10,850.824	315.514	
19	Lorentzian 17	922.094	10,844.881	309.571	
20	Lorentzian 18	923.499	10,828.382	293.072	289.00
21	Lorentzian 19	926.096	10,798.017	262.707	
22	Lorentzian 20	926.938	10,788.208	252.898	
23	Lorentzian 21	925.809	10,801.364	266.054	264.00
24	Lorentzian 22	928.568	10,769.271	233.961	228.00
25	Lorentzian 23	930.075	10,751.821	216.511	
26	Lorentzian 24	930.636	10,745.340	210.030	
27	Lorentzian 25	931.551	10,734.785	199.475	
28	Lorentzian 26	933.500	10,712.373	177.063	
29	Lorentzian 27	934.760	10,697.933	162.623	
30	Lorentzian 28	935.567	10,688.705	153.395	
31	Lorentzian 29	936.429	10,678.866	143.556	146.00
32	Lorentzian 30	937.207	10,670.001	134.691	137.00
33	Lorentzian 31	937.923	10,661.856	126.546	
34	Lorentzian 32	938.804	10,651.851	116.541	120.00
35	Lorentzian 33	940.000	10,638.298	102.988	98.00
36	Lorentzian 34	941.375	10,622.759	87.449	
37	Lorentzian 35	941.942	10,616.365	81.055	
38	Lorentzian 36	943.036	10,604.049	68.739	
39	Lorentzian 37	943.429	10,599.632	64.322	
40	Lorentzian 38	944.218	10,590.775	55.465	
41	Lorentzian 39	944.784	10,584.430	49.120	
42	Lorentzian 40	945.141	10,580.432	45.122	
43	Lorentzian 41	945.605	10,575.240	39.930	
44	Lorentzian 42	946.208	10,568.501	33.191	
45	Lorentzian 43	946.681	10,563.220	27.910	
46	Lorentzian 44	947.378	10,555.449	20.139	
47	Lorentzian 45	947.829	10,550.426	15.116	

Table 8 Compilation of all Yb:Lu$_2$O$_3$ electronic and vibrational transitions at 8 K

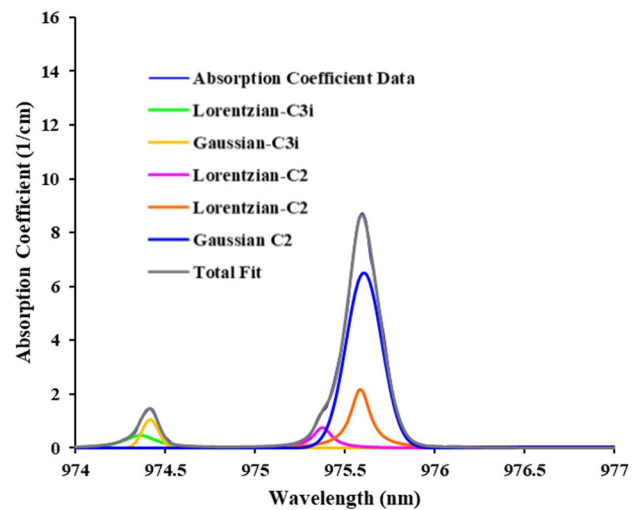| Transition number	Fitting function type	Center wavelength (nm)	Absorption coefficient (1/cm)	FWHM (nm)	Center wavenumber (cm^{-1})	Comments
1	Gaussian 1	880.677	0.022	1.263	11,354.901	C$_{3i}$ level
2	Lorentzian 1	895.770	0.032	3.640	11,163.580	
3	Lorentzian 2	898.424	0.040	1.440	11,130.602	
4	Lorentzian 3	902.830	1.000	2.980	11,076.282	C$_2$ level
5	Gaussian 2	903.907	0.508	1.086	11,063.085	
6	Lorentzian 4	905.215	0.360	1.244	11,047.099	
7	Lorentzian 5	906.509	0.288	2.094	11,031.330	
8	Lorentzian 6	907.902	0.091	1.418	11,014.405	
9	Lorentzian 7	909.434	0.055	1.840	10,995.850	
10	Lorentzian 8	912.382	0.162	3.368	10,960.321	
11	Lorentzian 9	913.802	0.057	0.662	10,943.290	
12	Lorentzian 10	915.092	0.105	1.702	10,927.863	
13	Lorentzian 11	916.115	0.063	1.328	10,915.660	
14	Lorentzian 12	917.301	0.096	2.290	10,901.547	
15	Lorentzian 13	918.810	0.058	0.874	10,883.643	
16	Lorentzian 14	919.885	0.119	1.492	10,870.924	
17	Lorentzian 15	920.460	0.017	0.414	10,864.133	
18	Lorentzian 16	921.589	0.099	1.908	10,850.824	
19	Lorentzian 17	922.094	0.033	0.416	10,844.881	
20	Lorentzian 18	923.499	0.067	1.120	10,828.382	
21	Lorentzian 19	926.096	0.091	2.254	10,798.017	
22	Lorentzian 20	926.938	0.055	0.940	10,788.208	
23	Lorentzian 21	925.809	0.070	2.118	10,801.364	
24	Lorentzian 22	928.568	0.499	0.700	10,769.271	
25	Lorentzian 23	930.075	0.297	1.842	10,751.821	
26	Lorentzian 24	930.636	0.033	0.452	10,745.340	
27	Lorentzian 25	931.551	0.121	0.758	10,734.785	
28	Lorentzian 26	933.500	0.204	1.298	10,712.373	
29	Lorentzian 27	934.760	0.817	1.200	10,697.933	
30	Lorentzian 28	935.567	0.157	0.932	10,688.705	
31	Lorentzian 29	936.429	0.142	0.900	10,678.866	
32	Lorentzian 30	937.207	0.127	0.980	10,670.001	
33	Lorentzian 31	937.923	0.264	0.556	10,661.856	
34	Lorentzian 32	938.804	0.282	0.688	10,651.851	
35	Lorentzian 33	940.000	0.369	2.334	10,638.298	
36	Lorentzian 34	941.375	0.159	0.850	10,622.759	C$_{3i}$ level
37	Lorentzian 35	941.942	0.115	0.526	10,616.365	
38	Lorentzian 36	943.036	0.410	0.578	10,604.049	
39	Lorentzian 37	943.429	0.339	0.974	10,599.632	
40	Lorentzian 38	944.218	0.472	0.986	10,590.775	
41	Lorentzian 39	944.784	0.158	0.464	10,584.430	
42	Lorentzian 40	945.141	0.249	0.572	10,580.432	
43	Lorentzian 41	945.605	0.791	0.692	10,575.240	
44	Lorentzian 42	946.208	0.395	0.666	10,568.501	
45	Lorentzian 43	946.681	0.378	0.558	10,563.220	
46	Lorentzian 44	947.378	1.050	0.572	10,555.449	
47	Lorentzian 45	947.829	0.645	0.812	10,550.426	
48	Lorentzian 46	948.647	0.816	0.538	10,541.329	
49	Lorentzian 47	948.930	0.831	0.290	10,538.185	

Table 8 (continued)

Transition number	Fitting function type	Center wavelength (nm)	Absorption coefficient (1/cm)	FWHM (nm)	Center wavenumber (cm^{-1})	Comments
50	Gaussian 3	949.189	6.868	0.250	10,535.310	C$_2$ (0, 1)–(1, 2) level, C$_2$ zero vibrational level (0,0)
51	Lorentzian 48	949.405	1.279	0.218	10,532.913	
52		957.500			10,443.864	Diffuse vibrational
53		964.350			10,369.679	Diffuse vibrational
54	Lorentzian 49	974.275	0.249	0.098	10,264.042	C$_{3i}$ zero level
55	Gaussian 4	974.408	0.991	0.126	10,262.642	C$_{3i}$ zero level
56	Lorentzian 50	974.422	0.420	0.084	10,262.494	C$_{3i}$ zero level
57	Lorentzian 51	975.371	0.904	0.116	10,252.509	C$_2$ zero level
58	Gaussian 5	975.584	1.604	0.068	10,250.271	C$_2$ zero level
59	Lorentzian 52	975.603	7.417	0.234	10,250.071	C$_2$ zero level
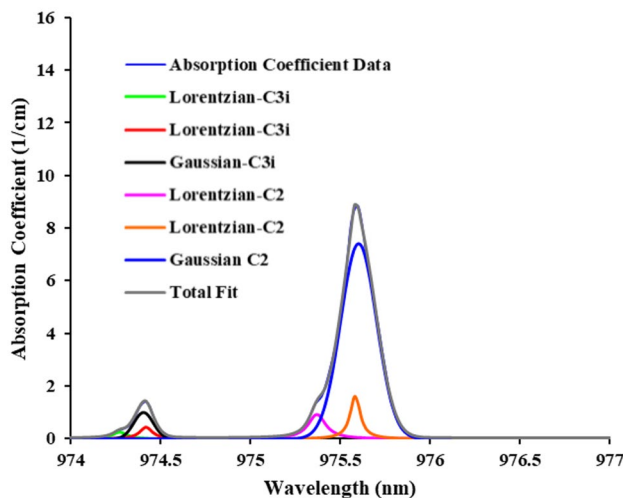
Fig. 14 Yb:Lu$_2$O$_3$ zero-phonon lines absorption data at 8 K, showing the C$_{3i}$ line on the left and the C$_2$ line on the right, as well as Gaussian and Lorentzian fits to the data

Fig. 15 Yb:Lu$_2$O$_3$ zero-phonon lines absorption data at 20 K, showing the C$_{3i}$ line on the left and the C$_2$ line on the right, as well as Gaussian and Lorentzian fits to the data

5.6 Complete compilation of all identified Yb:Lu$_2$O$_3$ transitions at 8 K

For convenience, we combined the data from Tables 6 and 7 into Table 8, and also added the diffuse transitions near 957.50 and 964.35 nm, and the fitting parameters for the C$_{3i}$ and C$_2$ zero-phonon lines, each of which could be decomposed to one Gaussian and two Lorentzian functions. The detailed zero-phonon spectra will be discussed in Sect. 5.6 of this paper. We can see, therefore, that the complete spectrum of Yb:Lu$_2$O$_3$ at 8 K consists of 59 discrete electronic and vibrational lines.

5.7 Zero phonon line region data and fits

Figures 14, 15, 16, 17, 18, 19, 20, 21, 22, 23, 24, 25 and 26 show the measured absorption coefficients at a range of temperatures from 8 to 300 K for the zero-phonon region of 974–977 nm. The region includes both the C$_2$ and C$_{3i}$ lines. We performed extensive fitting for each temperature, and found that excellent agreement between the experimental data and the fits can be obtained using Gaussian and Lorentzian fitting functions. For all cases examined the goodness of fit, as measured by the calculated χ^2 value, exceeded 99.9%. We did not examine whether equivalent or better fits might be obtained with a Voigt or other common functions. We note that the total fit and absorption coefficient data have a high degree of overlap, and in some of Figures 14, 15, 16,
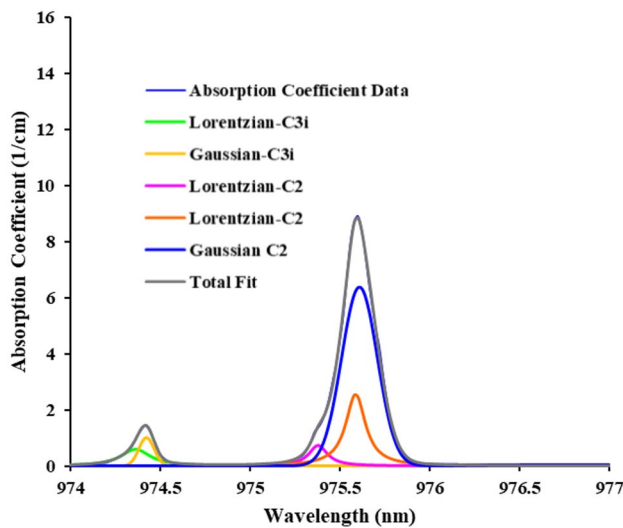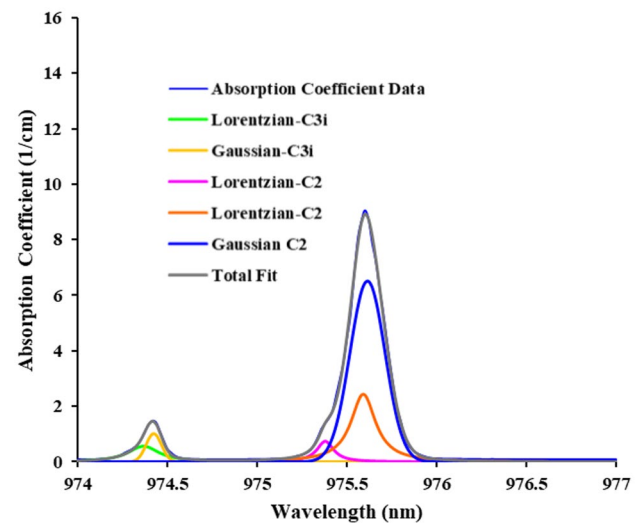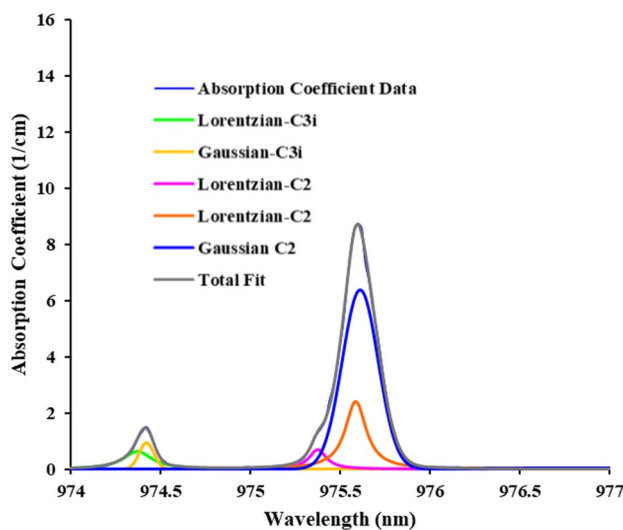
Fig. 16 $Yb:Lu_2O_3$ zero-phonon lines absorption data at 30 K, showing the C_{3i} line on the left and the C_2 line on the right, as well as Gaussian and Lorentzian fits to the data
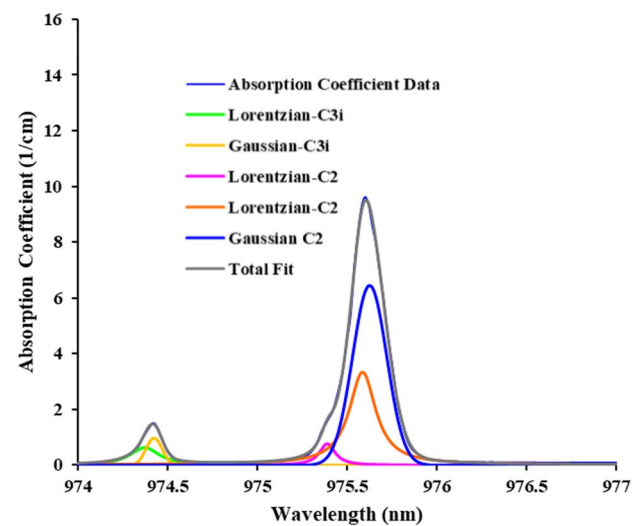

Fig. 18 $Yb:Lu_2O_3$ zero-phonon lines absorption data at 50 K, showing the C_{3i} line on the left and the C_2 line on the right, as well as Gaussian and Lorentzian fits to the data

Fig. 17 $Yb:Lu_2O_3$ zero-phonon lines absorption data at 40 K, showing the C_{3i} line on the left and the C_2 line on the right, as well as Gaussian and Lorentzian fits to the data

Fig. 19 $Yb:Lu_2O_3$ zero-phonon lines absorption data at 60 K, showing the C_{3i} line on the left and the C_2 line on the right, as well as Gaussian and Lorentzian fits to the data

17, 18, 19, 20, 21, 22, 23, 24, 25 and 26 are indistinguishable from one another. Table 9 lists, for each temperature, the site type, fitting function type, and the center wavelength, FWHM bandwidth, and absorption coefficient for each individual function.

The fitting function parameters of Table 9 can be used to generate a number of interesting plots, and to provide for the first time a detailed look at the variation in parameters with temperature for both the C_2 and C_{3i} transitions. Figure 27 shows the absorption coefficient and FWHM bandwidth as a function of temperature for the Gaussian component

of the C_2 line. The Gaussian component corresponds, we believe, to the pure electronic part of the linewidth, and is maximum at 8 K. It gradually decreases to about 100 K, and then dramatically reduces in intensity between 100 and 150 K, remaining constant thereafter. The FWHM bandwidth is seen to remain constant up to about 100 K, and then to continually increase up to 300 K. In Fig. 28, we show the C_2 Lorentzian absorption coefficient and FWHM bandwidth; the Lorentzian component, that we believe to be primarily a measure of the thermal part of the bandwidth, increases beginning at the lowest temperatures monotonically until
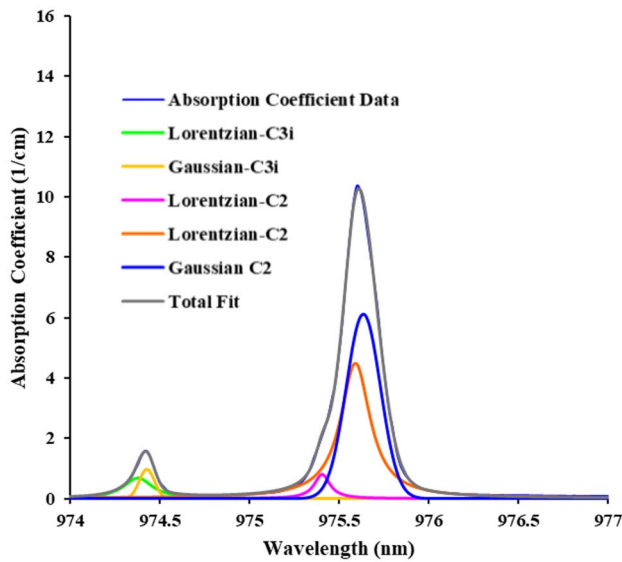
Fig. 20 Yb:Lu$_2$O$_3$ zero-phonon lines absorption data at 70 K, showing the C$_{3i}$ line on the left and the C$_2$ line on the right, as well as Gaussian and Lorentzian fits to the data
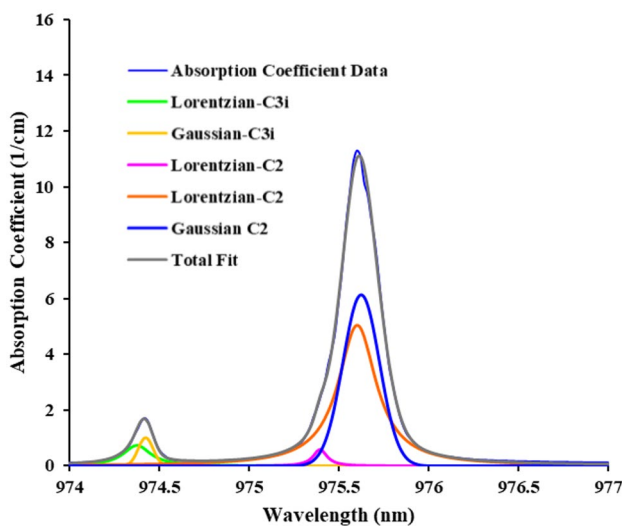

Fig. 22 Yb:Lu$_2$O$_3$ zero-phonon lines absorption data at 100 K, showing the C$_{3i}$ line on the left and the C$_2$ line on the right, as well as Gaussian and Lorentzian fits to the data

Fig. 21 Yb:Lu$_2$O$_3$ zero-phonon lines absorption data at 80 K, showing the C$_{3i}$ line on the left and the C$_2$ line on the right, as well as Gaussian and Lorentzian fits to the data

Fig. 23 Yb:Lu$_2$O$_3$ zero-phonon lines absorption data at 150 K, showing the C$_{3i}$ line on the left and the C$_2$ line on the right, as well as Gaussian and Lorentzian fits to the data

90 K, where a sudden drop occurs. Thereafter, the intensity increases to 150 K, where the intensity decreases dramatically up to 300 K. The FWHM bandwidth also increases up to 90 K where a sudden drop occurs, and thereafter substantially increases up to 300 K. In Fig. 29, we plot the absorption coefficient and FWHM intensity for the smaller Lorentzian C$_2$ component located at 975.371 nm at 8 K. This transition gradually reduces in intensity and increases in bandwidth until 80 K, whereupon it disappears completely up to 300 K. This transition is likely the result of a C$_2$–C$_2$
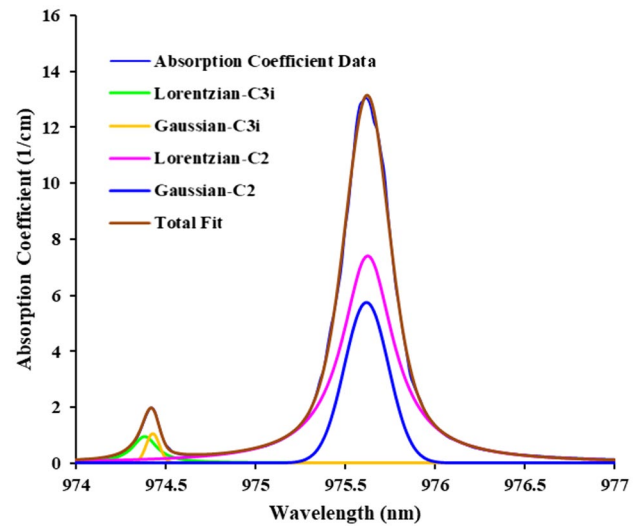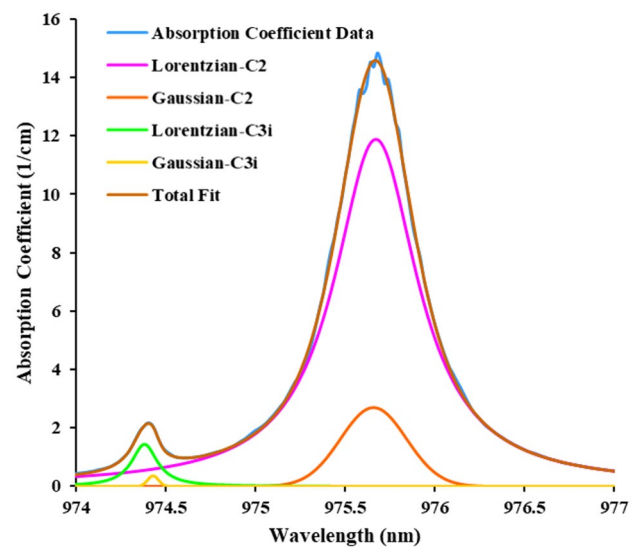
cation nearest-neighbor interaction, resulting in a Stokes shifted component, as has been found recently by Guzik et al. [25]. Because the nearest-neighbor interaction is not strong for Yb:Lu$_2$O$_3$, the Stokes shift occurs inside the zero-line profile, unlike for Nd:Lu$_2$O$_3$ where the Stokes shifted line may be found in the shoulder of the zero-line profile [25]. In Fig. 30, the absorption coefficient and FWHM bandwidth are plotted for the main Gaussian electronic part of the C$_{3i}$ forbidden line. The absorption coefficient and bandwidth are seen to be more or less constant until between 100 and
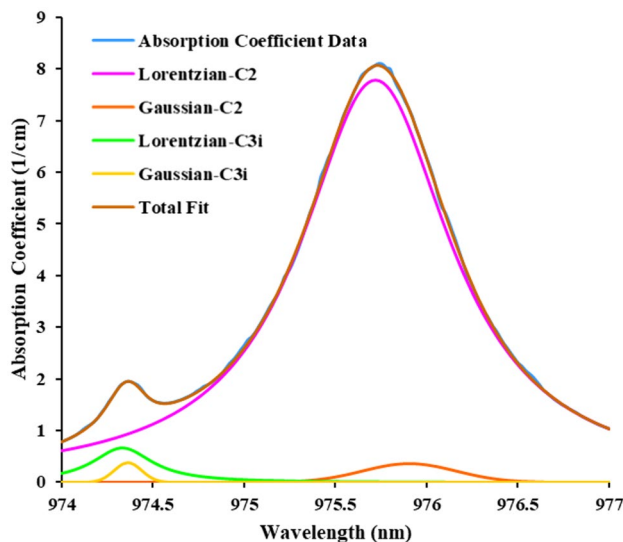
Fig. 24 Yb:Lu$_2$O$_3$ zero-phonon lines absorption data at 200 K, showing the C$_{3i}$ line on the left and the C$_2$ line on the right, as well as Gaussian and Lorentzian fits to the data
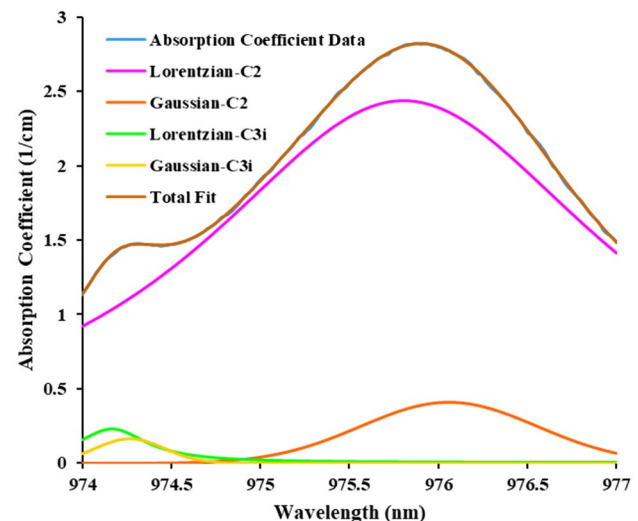

Fig. 25 Yb:Lu$_2$O$_3$ zero-phonon lines absorption data at 250 K, showing the C$_{3i}$ line on the left and the C$_2$ line on the right, as well as Gaussian and Lorentzian fits to the data
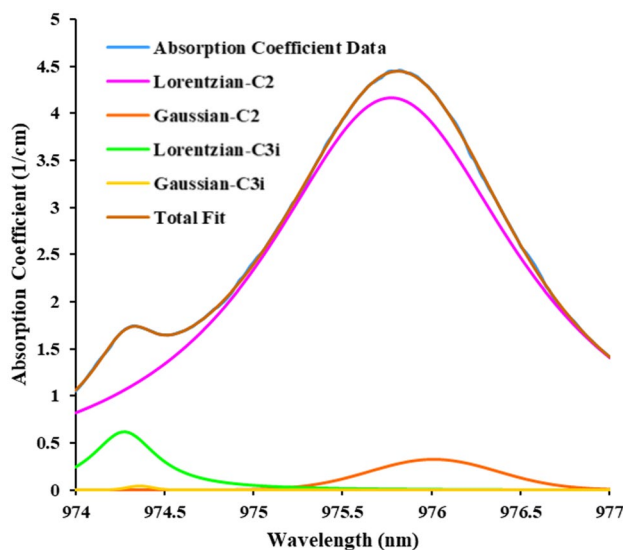
150 K where a dramatic drop in the C$_{3i}$ Gaussian intensity takes place, while the FWHM bandwidth increases beyond 150 K, and becomes very large at 300 K. The behavior of the C$_{3i}$ Gaussian transition and the C$_2$ Gaussian transition (Fig. 27) are in fact very similar. For the C$_{3i}$ main Lorentzian transition, shown in Fig. 31, we see a gradual increase in the absorption coefficient intensity up to 100 K, a large increase between 100–150 K, and then thereafter a dramatic decrease up to 300 K. The FWHM bandwidth gradually decreases

Fig. 26 Yb:Lu$_2$O$_3$ zero-phonon lines absorption data at 300 K, showing the C$_{3i}$ line on the left and the C$_2$ line on the right, as well as Gaussian and Lorentzian fits to the data

until about 100 K, and then at 150 K begins to increase substantially up to 300 K. The behavior is thus very similar to the C$_2$ Lorentzian data of Fig. 28.

In Fig. 32, we use the fitting functions for the zero-lines summarized in Table 9 to calculate the total (whether C$_2$ or C$_{3i}$) Gaussian and Lorentzian areas for each temperature, and the sum of the Gaussian and Lorentzian areas to find the total area. It is clear that at about 80–90 K, the nature of the zero-line changes from being primarily Gaussian to being predominantly Lorentzian with an intensity that exceeds the Gaussian intensity up to 300 K.

Figures 27, 28, 29, 30, 31 and 32 offer a comprehensive view of the many interesting changes that accompany the Lu$_2$O$_3$ structure as temperature is varied. The disappearance of the C$_{3i}$ small Stokes-shifted Lorentzian component at 80 K is very likely the result of the thermal expansion of the unit cell as temperature increases, which increases the nearest-neighbor distances of the cations. This view is supported by the near equality of the Gaussian and Lorentzian areas that occurs near 100 K, and the growth of Lorentzian (thermal) contributions to the linewidth over Gaussian (electronic) contributions beyond 100 K. Due to the thermal expansion of the unit cell, and the resulting changes to the local coordination environment, it also seems clear that the local crystalline field experienced by each Lu cation in the C$_2$ site becomes weaker as temperature rises. The reduced local field can be attributed, at least partially to thermal expansion, or to changes resulting from a change in the local (distorted) environment. Between 80 and 100 K, it appears that a soft phase-transition involving the rearrangement of the local coordination environment may be taking place, resulting in a reduced local field and a lower

Table 9 Fitting function parameters for C$_{3i}$ and C$_2$ sites for each temperature measured, showing fit type [Lorentzian (L) and Gaussian (G)]

T (K)	Site	Fitting type	λ_0 (nm)	$\Delta\lambda_{FWHM}$ (nm)	α (1/cm)
8	C$_{3i}$	L	974.275	0.097	0.249
	C$_{3i}$	G	974.408	0.127	0.991
	C$_{3i}$	L	974.422	0.084	0.042
	C$_2$	L	975.371	0.117	0.904
	C$_2$	L	975.584	0.068	1.604
	C$_2$	G	975.603	0.234	7.417
20	C$_{3i}$	L	974.362	0.218	0.489
	C$_{3i}$	G	974.419	0.106	1.073
	C$_2$	L	975.376	0.126	0.771
	C$_2$	L	975.587	0.130	2.198
	C$_2$	G	975.606	0.233	6.513
30	C$_{3i}$	L	974.364	0.197	0.592
	C$_{3i}$	G	974.425	0.100	0.998
	C$_2$	L	975.379	0.124	0.754
	C$_2$	L	975.587	0.132	2.542
	C$_2$	G	975.608	0.234	6.388
40	C$_{3i}$	L	974.373	0.195	0.635
	C$_{3i}$	G	974.423	0.096	0.949
	C$_2$	L	975.375	0.116	0.714
	C$_2$	L	975.586	0.140	2.425
	C$_2$	G	975.611	0.234	6.382
50	C$_{3i}$	L	974.369	0.210	0.563
	C$_{3i}$	G	974.426	0.100	1.015
	C$_2$	L	975.379	0.112	0.734
	C$_2$	L	975.591	0.166	2.453
	C$_2$	G	975.615	0.229	6.534
60	C$_{3i}$	L	974.374	0.199	0.612
	C$_{3i}$	G	974.426	0.105	0.954
	C$_2$	L	975.390	0.104	0.771
	C$_2$	L	975.586	0.178	3.332
	C$_2$	G	975.626	0.223	6.442
70	C$_{3i}$	L	974.380	0.194	0.675
	C$_{3i}$	G	974.430	0.099	0.977
	C$_2$	L	975.406	0.104	0.819
	C$_2$	L	975.591	0.199	4.502
	C$_2$	G	975.635	0.224	6.110
80	C$_{3i}$	L	974.378	0.186	0.736
	C$_{3i}$	G	974.426	0.098	1.015
	C$_2$	L	975.395	0.093	0.574
	C$_2$	L	975.602	0.257	5.045
	C$_2$	G	975.624	0.239	6.132
90	C$_{3i}$	L	974.382	0.184	0.769
	C$_{3i}$	G	974.425	0.093	1.076
	C$_2$	L	975.395	0.132	0.800
	C$_2$	L	975.636	0.426	3.282
	C$_2$	G	975.618	0.246	8.739

Table 9 (continued)

T (K)	Site	Fitting type	λ_0 (nm)	$\Delta\lambda_{FWHM}$ (nm)	α (1/cm)
100	C$_{3i}$	L	974.385	0.166	0.964
	C$_{3i}$	G	974.430	0.087	1.054
	C$_2$	L	975.625	0.347	7.414
	C$_2$	G	975.618	0.288	5.755
150	C$_{3i}$	L	974.384	0.173	1.439
	C$_{3i}$	G	974.432	0.070	0.346
	C$_2$	L	975.672	0.566	11.890
	C$_2$	G	975.659	0.431	2.706
200	C$_{3i}$	L	974.334	0.400	0.658
	C$_{3i}$	G	974.364	0.177	0.377
	C$_2$	L	975.719	1.000	7.781
	C$_2$	G	975.903	0.603	0.356
250	C$_{3i}$	L	974.274	0.444	0.622
	C$_{3i}$	G	974.361	0.168	0.041
	C$_2$	L	975.773	1.748	4.162
	C$_2$	G	976.011	0.844	0.326
300	C$_{3i}$	L	974.167	0.481	0.228
	C$_{3i}$	G	974.267	0.46	0.163
	C$_2$	L	975.804	2.805	2.442
	C$_2$	G	976.059	1.167	0.408

λ_0 center wavelength, $\Delta\lambda_{FWHM}$ the FWHM bandwidth, α absorption coefficient

electronic transition probability. To examine this we conducted a series of low temperature X-ray diffraction experiments described in Sect. 6.0 of this paper, and discovered that subtle but apparently important changes in the structure are indeed occurring.

6 X-ray analysis of Lu$_2$O$_3$ coordination environments

To help determine the cause of the unusual low temperature absorption behavior, we obtained full single-crystal data sets at a range of temperatures between 100 and 300 K by single-crystal X-ray diffraction. We wished to test whether there was any detectable distortion or symmetry reduction/alteration about the Lu sites that could be leading to the observed optical effects. We obtained good quality structure refinements consistent with the bixbyite structure type, and did not observe deviations in site symmetry or space group as a function of temperature. As expected, the lattice parameter contracts as a function of lower temperatures (Fig. 33), but we did not observe any preferential contraction/expansion of the Lu–O bond lengths that resulted in any change in site symmetry. We do, however, observe an unusual structural curiosity around 150 K. At these lower temperatures, the structure

Fig. 27 C_2 zero-line (975.603 nm at 8 K) electronic Gaussian absorption coefficient and FWHM bandwidth as a function of temperature as determined by least-squares fitting to experimental data
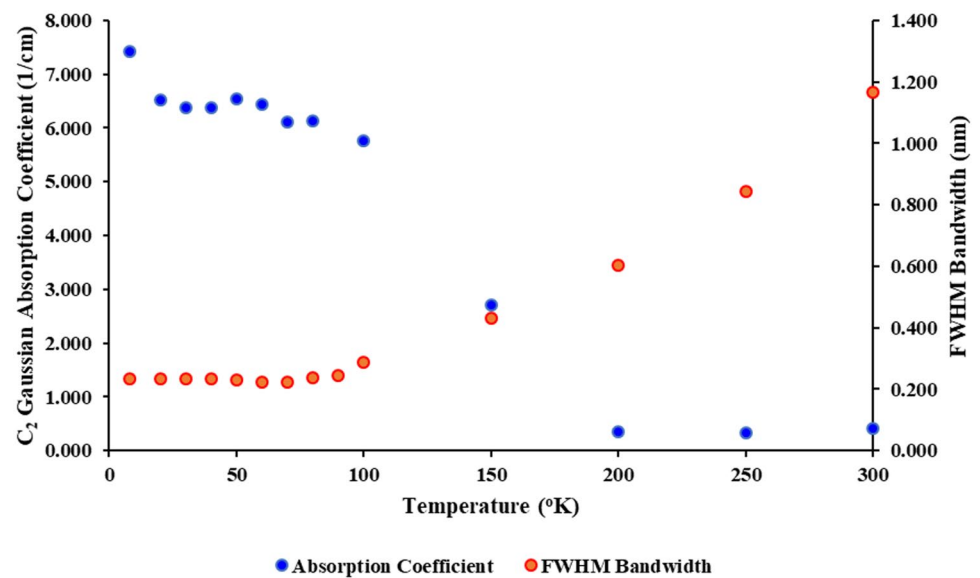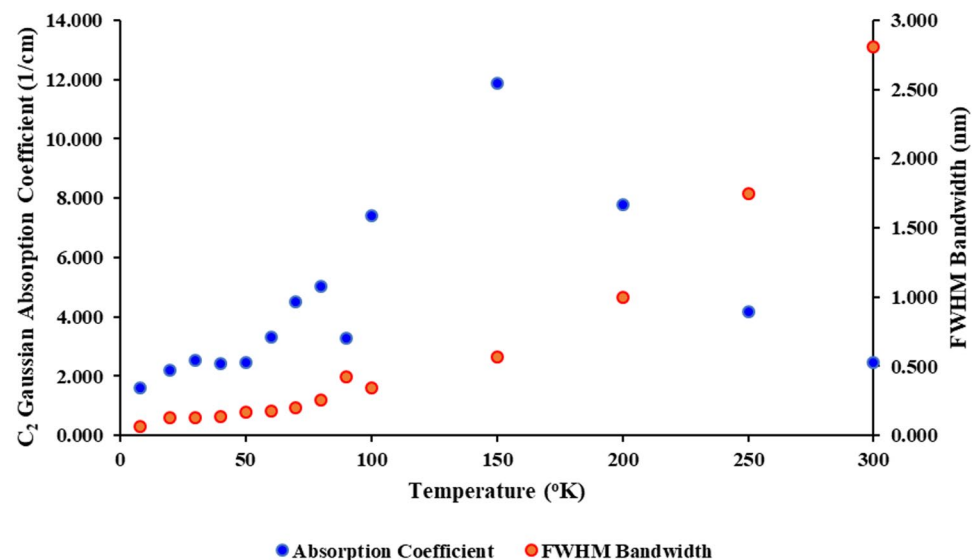

Fig. 28 C_2 zero-line (975.584 nm at 8 K) main Lorentzian absorption coefficient and FWHM bandwidth as a function of temperature as determined by least-squares fitting to experimental data

refinement was significantly improved by switching the Lu1 atom (which is the centrosymmetric C_{3i} site) from the 8b Wyckoff site above 150 K to the 8a Wyckoff site at and below 150 K. The symmetry does not change, but this positional switch also causes the Lu2 site to move to a different 24d site (still having C_2 symmetry), and the oxygen atom likewise moves to a different 48e site (Table 10). Both models (above and below 150 K) have the same local arrangements of atoms, but the structure refines significantly better when the specific arrangements are used for higher temperatures versus lower temperatures. This curious phenomenon was observed for multiple crystals tested in the same temperature range. Both arrangements are reported in the literature for oxides of the bixbyite structure type [17, 26–28]. We are not yet sure if this is a

contributing factor to the observed optical properties that occur at or near the same temperature, but decided it at least warranted mention here.

7 Discussion and conclusions

In this paper, we have presented the results of a comprehensive study of the variation of the detailed spectroscopic absorption properties of the laser material $Yb:Lu_2O_3$ as temperature is varied between 8 and 300 K. Because of the wide range of temperatures used in our measurements, it is now possible to see in a glance the evolution of the general absorption features as a function of temperature. Our measurements, when combined with the detailed fitting functions,

Fig. 29 C$_2$ zero-line (975.371 nm at 8 K) C$_2$–C$_2$ Stokes Lorentzian absorption coefficient and FWHM bandwidth as a function of temperature as determined by least-squares fitting to experimental data
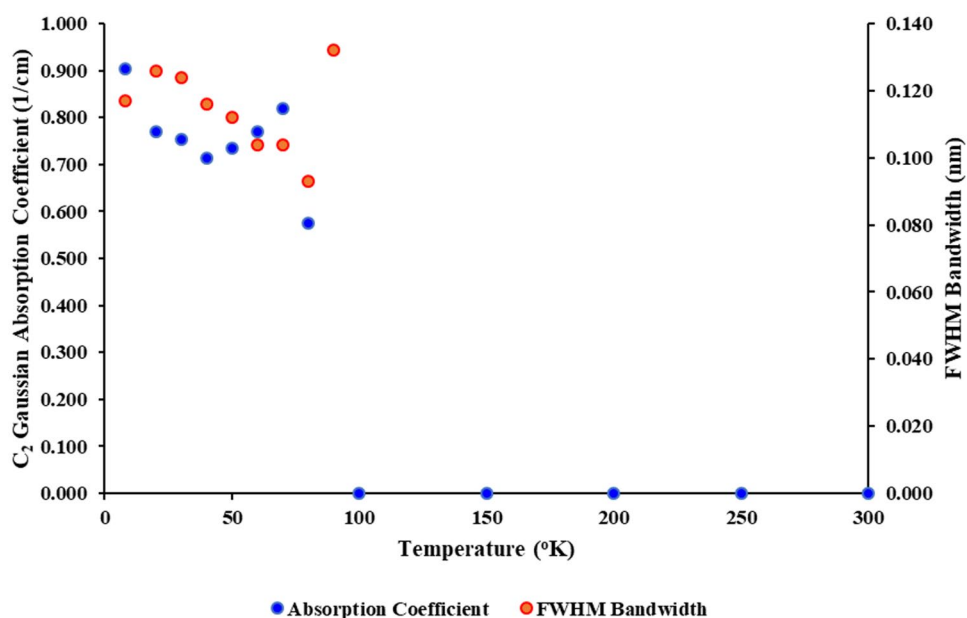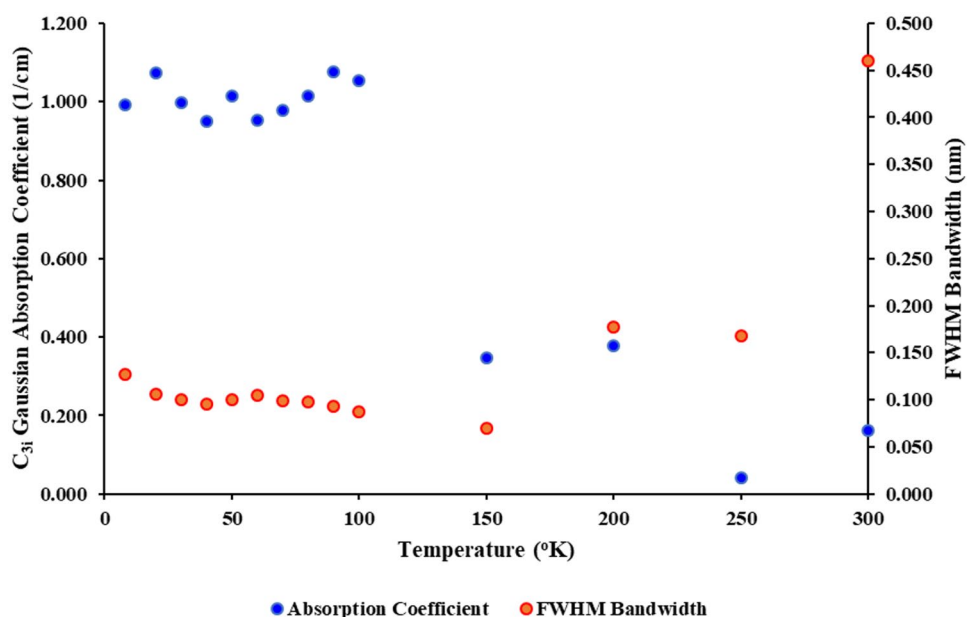

Fig. 30 C$_{3i}$ zero-line (974.408 nm at 8 K) electronic Gaussian absorption coefficient and FWHM bandwidth as a function of temperature as determined by least-squares fitting to experimental data

and a least-squares approach to fitting the experimental data, also yielded many fine details of the observed electronic-vibrational transitions, and of the zero-line data.

We experimentally observed for the first time, the C$_{3i}$ (0, 1)–(1, 3) transition at 880.7 nm at 8 K, and based on the detailed high confidence fits to the experimental data, present for the first time a compilation of all 59 electronic and vibrational transitions observed, including the center wavelength, bandwidth, and absorption coefficient amplitude. Our high-resolution zero-line data make it possible to observe the detailed relationship of the C$_2$ and C$_{3i}$ zero-lines, and the way in which they merge at higher temperatures. Detailed fitting of the zero-lines also allowed

us to identify for the first time a C$_2$ satellite Stokes transition attributable to nearest-neighbor cation interactions, which disappears at about 80 K and is unobservable at higher temperatures. Through detailed modeling of the zero linewidths, we observed the evolution of individual lines with temperature for both the C$_2$ and C$_{3i}$ sites. They also show the progression of the linewidth from having a mostly electronic (Gaussian) nature below 100 K to being dominated by thermal processes (Lorentzian) at higher temperatures. When taken as a whole, it is clear from the data that something significant happens to the Yb^{3+} ion in the lattice between 80–100 K, and we identified a "soft" phase-transition from our X-ray measurements of

Fig. 31 C_{3i} zero-line (974.275 nm at 8 K) Lorentzian absorption coefficient and FWHM bandwidth as a function of temperature as determined by least-squares fitting to experimental data
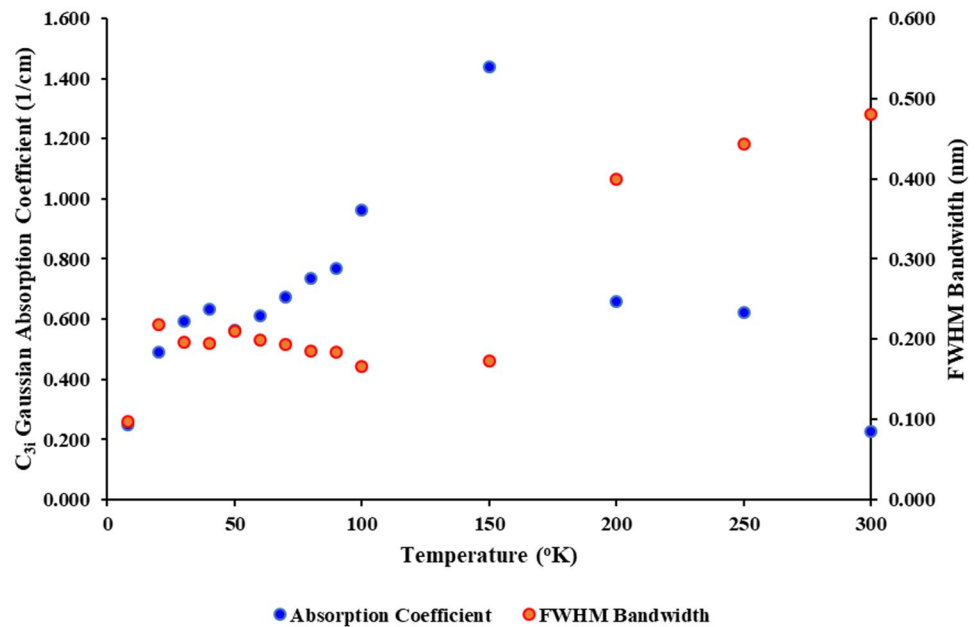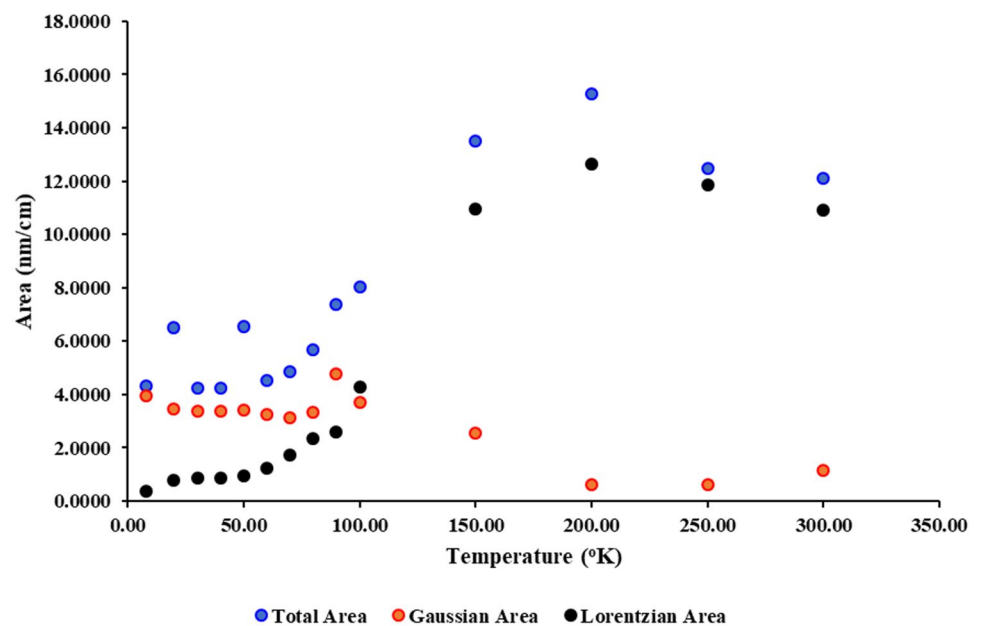

Fig. 32 Gaussian, Lorentzian, and total transition area as a function of temperature

the coordination environment that support this conclusion. Furthermore, recently, a closely related crystal, $Yb:Y_2O_3$, has been found to behave in a very similar way, with the total area of the zero-line varying in much the same way as shown here for $Yb:Lu_2O_3$ (Fig. 32) [29]. In our study, a single hydrothermally grown laser crystal was used, whereas in [29], the samples were ceramic. This close similarity between the two results reduces the likelihood that the variation in the zero-line strength is due to some growth-related strain or to an inadvertent impurity.

Fig. 33 Yb:Lu$_2$O$_3$ lattice parameter as a function of temperature. Data are fit to linear (blue) and polynomial (red) trendlines
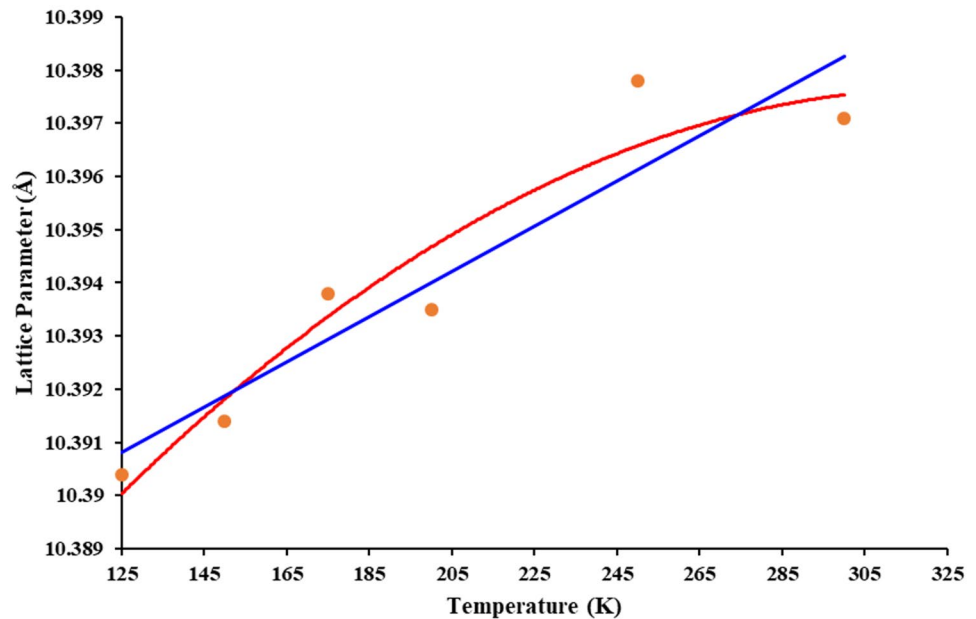

Table 10 Positional parameters as a function of temperature

Temp (K)	Lu1 x	Lu1 y	Lu1 z	Lu2 x	Lu2 y	Lu2 z	O1 x	O1 y	O1 z
300	0.25	0.25	0.25	0.25	0.533124	0.5	0.152454	0.379955	0.391585
250	0.25	0.25	0.25	0.25	0.533171	0.5	0.152882	0.379828	0.391229
200	0.25	0.25	0.25	0.25	0.533163	0.5	0.153893	0.380065	0.391276
175	0.25	0.25	0.25	0.25	0.533168	0.5	0.152795	0.380431	0.391802
150	0.5	0.5	0.5	0.25	0.716776	0.5	0.870326	0.902874	0.641553
125	0.5	0.5	0.5	0.25	0.716813	0.5	0.870062	0.903069	0.641588

References

1. K. Petermann, G. Huber, L. Fornasiero, S. Kuch, E. Mix, V. Peters, S.A. Basun, Rare-earth-doped sesquioxides. J. Lumin. **87–89**, 973–975 (2000)
2. V. Peters, Growth and spectroscopy of ytterbium-doped sesquioxides, PhD Dissertation, University of Hamburg 2001
3. K. Petermann, L. Fornasiero, E. Mix, V. Peters, High melting sesquioxides: crystal growth, spectroscopy, and laser experiments. Opt. Mater. **19**, 67–71 (2002)
4. R. Peters, C. Krankel, K. Petermann, G. Huber, Broadly tunable high-power Yb:Lu$_2$O$_3$ thin disk laser with 80% slope efficiency. Opt. Express **15**, 7076–7082 (2007)
5. U. Grieber, V. Petrov, K. Petermann, V. Peters, Passively mode-locked Yb:Lu$_2$O$_3$ laser. Opt. Express **12**, 3125–3130 (2004)
6. M. Tokurakawa, A. Shirakawa, K. Ueda, H. Yagi, S. Hosokawa, T. Yanagitani, A.A. Kaminskii, Diode-pumped 65 fs Kerr-lens mode-locked Yb^{3+}:Lu$_2$O$_3$ and nondoped Y$_2$O$_3$ combined ceramic laser. Opt. Lett. **33**, 1380–1382 (2008)
7. N. Modsching, J. Drs, J. Fischer, C. Paradis, F. Labaye, M. Gaponenko, C. Krankel, V. Wittwer, T. Sudmeyer, Sub-100-fs Kerr lens mode-locked Yb:Lu$_2$O$_3$ thin-disk laser oscillator operating at 21 W average power. Opt. Express **27**, 16111 (2019)
8. K. Takaichi, H. Yagi, A. Shirakawa, K. Ueda, S. Hosokawa, T. Yanagitani, A.A. Kaminskii, Lu$_2$O$_3$:Yb^{3+} ceramics—a novel gain material for high-power solid-state lasers. Phys. Stat. Solidi (a) **202**, R1–R3 (2005)
9. A.A. Kaminskii, S.N. Bagayev, K. Ueda, K. Takaichi, A. Shirakawa, S.N. Ivanov, E.N. Khazanov, A.V. Taranov, H. Yagi, T. Yanagitani, New results on characterization of highly transparent C-modification Lu$_2$O$_3$ nanocrystalline ceramics: room-temperature tunable CW laser action of Yb^{3+} ions under LD-pumping and the propagation kinetics of non-equilibrium acoustic phonons. Laser Phys. Lett. **3**, 375–379 (2006)
10. A. Pirri, G. Toci, M. Vannini, First laser oscillation and broad tunability of 1 at% Yb- doped Sc$_2$O$_3$ and Lu$_2$O$_3$ ceramics. Opt. Lett. **36**, 4284–4286 (2011)
11. J. Sanghera, W. Kim, C. Baker, G. Villalobos, J. Frantz, B. Shaw, A. Lutz, B. Sadowski, R. Miklos, M. Hunt, F. Kung, I. Aggarwal, Laser oscillation in hot pressed 10% Yb^{3+}:Lu$_2$O$_3$ ceramic. Opt. Mater. **33**, 670–674 (2011)
12. D. Yin, J. Ma, P. Liu, B. Yao, J. Wang, Z. Dong, L.B. Kong, D. Tang, Submicron-grained Yb:Lu$_2$O$_3$ transparent ceramics with lasing quality. J. Am. Ceram. Soc. **102**, 2587–2592 (2019)
13. C. McMillen, D. Thompson, T. Tritt, J. Kolis, Hydrothermal single-crystal growth of Lu$_2$O$_3$ and lanthanide-doped Lu$_2$O$_3$. Cryst. Growth. Des. **11**, 4386–4391 (2011)
14. D.C. Brown, C.D. McMillen, C. Moore, J.W. Kolis, V. Envid, Spectral properties of hydrothermally-grown Nd:LuAG, Yb:LuAG, and Yb:Lu$_2$O$_3$ laser materials. J. Lumin. **148**, 26–32 (2014)

15. C.A. Moore, D.C. Brown, L.D. Sanjeewa, C.D. McMillen, J.W. Kolis, "Yb:Lu$_2$O$_3$ hydrothermally-grown single-crystal and ceramic absorption spectra obtained between 298 and 80 K. J. Lumin. **174**, 29–35 (2016)

16. C.D. McMillen, L.D. Sanjeewa, C.A. Moore, D.C. Brown, J.W. Kolis, Crystal growth and phase stability of Ln:Lu$_2$O$_3$ (Ln=Ce, Pr, Nd, Sm, Eu, Tb, Dy, Ho, Er, Tm, Yb) in a higher temperature hydrothermal regime. J. Cryst. Growth **452**, 146–150 (2016)

17. M. Guzik, J. Pejchal, A. Yoshikawa, A. Ito, T. Goto, M. Siczek, T. Lis, G. Boulon, Structural investigations of Lu$_2$O$_3$ as single crystal and transparent ceramic. Cryst. Growth Des. **14**, 3327–3334 (2014)

18. D.E. Zelmon, J.M. Northridge, N.D. Haynes, D. Perlov, K. Petermann, Temperature-dependent Sellmeier equations for rare-earth sesquioxides. Appl. Opt. **52**, 3824–3827 (2013)

19. H.H. Li, J. Phys. Chem. Ref. Data **9**, 161–289 (1980)

20. M. Orrit, Single molecular spectroscopy, in *Quantum optics and nanophysics*, ed. by C. Fabry, V. Sandoghdan, N. Treps, L.F. Cugliandolo (Oxford University Press, Oxford, 2017)

21. Y. Guyot, M. Gusik, G. Alombert-Goget, J. Pejchl, A. Yoshikawa, A. Ito, T. Goto, G. Boulon, "Assignment of Yb^{3+} energy levels in the C$_2$ and C$_{3i}$ centers of Lu$_2$O$_3$ sesquioxide either as ceramics or as crystal. J. Lumin. **170**, 513–519 (2016)

22. A. Lupei, A. Lupei, C. Presura, V.N. Enaki, A. Petraru, Electron-phonon coupling effects on Yb^{3+} spectra in several laser crystals. J. Phys. Condens. Matter **11**, 3769–3778 (1999)

23. L. Laversenne, Y. Guyot, C. Goutaudier, MTh Cohen-Adad, G. Boulon, Optimization of spectroscopic properties of Yb^{3+}-doped refractory sesquioxides: cubic Y$_2$O$_3$, Lu$_2$O$_3$, and monoclinic Gd$_2$O$_3$. Opt. Mater. **16**, 475–483 (2001)

24. M.V. Abrashev, N.D. Todorov, J. Geshev, Raman spectra of R$_2$O$_3$ (R-rare earth) sesquioxides with C-type bixbyite crystal structure: a comparative study. J. Appl. Phys. **116**, 103508-1–103508-6 (2014)

25. M. Guzik, G. Alombert-Goget, Y. Guyot, J. Pejchal, A. Yoshikawa, A. Ito, T. Goto, G. Boulon, "Spectroscopy of C$_{3i}$ and C$_2$ sites of Nd^{3+}-doped Lu$_2$O$_3$ sesquioxide either as ceramics or crystal. J. Lumin. **169**, 606–611 (2016)

26. S. Geller, Structures of α-Mn$_2$O$_3$, (Mn$_{0.983}$Fe$_{0.017}$)$_2$O$_3$ and (Mn$_{0.37}$Fe$_{0.63}$)$_2$O$_3$ and relation to magnetic ordering. Acta Cryst. **B27**, 821–828 (1971)

27. L. Pauling, M. Shappell, The crystal structure of bixbyite and the C-modification of the sesquioxides. Z. Kristallogr. **75**, 128–142 (1930)

28. H. Kohlmann, The crystal structure of cubic C-type samarium sesquioxide, Sm$_2$O$_3$. Z. Naturforsch. B **74**, 433–435 (2019)

29. L.D. Merkle, G.A. Newburgh, N. Ter-Gabrielyan, A. Michael, M. Dubinskii, Temperature-dependent lasing and spectroscopy of Yb:Y$_2$O$_3$ and Yb:Sc$_2$O$_3$. Opt. Commun. **281**, 5855–5861 (2008)